



Article

Cite this article: Carr JR, Barrett A, Rinzin S, Taylor C (2025). Step-change in supraglacial pond area on Tshojo Glacier, Bhutan, and potential downstream inundation patterns due to pond drainage events. *Journal of Glaciology* **71**, e9, 1–19. <https://doi.org/10.1017/jog.2024.62>

Received: 5 January 2024

Revised: 19 July 2024

Accepted: 24 July 2024

Key words:

climate change; debris-covered glaciers; glacier hazards; glacier hydrology; mountain glaciers

Corresponding author:

J. Rachel Carr;

Email: Rachel.carr@newcastle.ac.uk

Step-change in supraglacial pond area on Tshojo Glacier, Bhutan, and potential downstream inundation patterns due to pond drainage events

J. Rachel Carr, Amy Barrett, Sonam Rinzin and Caroline Taylor 

School of Geography, Politics and Sociology, Newcastle University, Newcastle, UK

Abstract

Climate change is causing Himalayan glaciers to shrink rapidly and natural hazards to increase, while downstream exposure is growing. Glacier shrinkage promotes the formation of glacial lakes, which can suddenly drain and produce glacier lake outburst floods (GLOFs). Bhutan is one of the most vulnerable countries globally to these hazards. Here we use remotely sensed imagery to quantify changes in supraglacial water storage on Tshojo Glacier, Bhutan, where previous supraglacial pond drainage events have necessitated downstream evacuation. Results showed a doubling of both total ponded area (104 529 m² to 213 943 m²) and its std dev. (64 808 m² to 158 550 m²) between the periods 1987–2003 and 2007–2020, which was predominantly driven by increases in the areas of the biggest ponds. These ponds drained regularly and have occupied the same location since at least 1967. Tshojo Glacier has remained in the first stage of proglacial lake development for 53 years, which we attribute to its moderate slopes and ice velocities. Numerical modelling shows that pond outbursts can reach between ~6 and 47 km downstream, impacting the remote settlement of Lunana. Our results highlight the need to better quantify variability in supraglacial water storage and its potential to generate GLOFs, as climate warms.

1. Introduction

Glaciers in High Mountain Asia (HMA) contain ~98 000 km² of ice (Millan and others, 2022), making them the largest ice mass outside the polar regions. These glaciers have been losing mass in recent decades at a rate of $-19.0 \pm 2.5 \text{ Gt a}^{-1}$ ($-0.19 \pm 0.03 \text{ m w.e. a}^{-1}$) between 2000 and 2018 (Shean and others, 2020), and this ice loss is forecast to continue during the 21st century (Rounce and others, 2020). Glacier mass balance has been particularly negative across central and eastern regions of the Himalaya and has coincided with rising air temperatures (e.g. Bolch and others, 2012; Brun and others, 2017; Maurer and others, 2019b; Shean and others, 2020; Hugonnet and others, 2021). Quantifying Himalayan glacier loss is crucial, as these glaciers are the source of Asia's largest river systems and ~220 million people depend on glacier melt to maintain water supplies throughout the dry season (e.g. Immerzeel and others, 2010; Pritchard, 2019; Immerzeel and others, 2020; Nie and others, 2021). Consequently, downstream populations are highly vulnerable to climate change-induced changes in glacial meltwater provision. Furthermore, populations in HMA are the most vulnerable globally to Glacial Lake Outburst Floods (GLOFs) (Carrivick and Tweed, 2016; Taylor and others, 2023), which occur when water impounded behind a natural dam (e.g. a moraine) is suddenly released (e.g. Fujita and others, 2013; Westoby and others, 2015). GLOFs can rapidly generate large volumes of water and sediment, which can cause major damage to downstream infrastructure, property and agricultural land, and loss of life (e.g. Carrivick and Tweed, 2016; Huggel and others, 2020; Zheng and others, 2021b; Emmer and others, 2022). Rapid ice loss has led to a dramatic increase in the number and volume of glacial lakes globally in recent years (Shugar and others, 2020), and this has been particularly marked in the eastern Himalaya (e.g. Komori, 2008; Wang and others, 2015; Watson and others, 2016; Zheng and others, 2021a). Given the potential impacts on water supplies and natural hazards, there is therefore an urgent need to quantify recent changes in glacial water storage in the eastern Himalaya.

GLOFs can occur from water impounded at the front/margins of glaciers or on their surface, and can be triggered by a variety of mechanisms, including: (i) failure of the dam impounding the lake; (ii) drainage of supraglacial ponds supra- or englacially; (iii) inputs from surrounding hillslopes and/or glaciers; (iv) ice calving and/or rapid meltwater inputs; (v) earthquakes; (vi) intense rainfall and/or high temperatures (e.g. Richardson and Reynolds, 2000; Westoby and others, 2014; Westoby and others, 2015; Rounce and others, 2016; Emmer and others, 2022; Shrestha and others, 2023). Supraglacial ponds also enhance ablation, by absorbing solar radiation and transmitting it to exposed ice (e.g. Quincey and others, 2007; Komori, 2008; Carrivick and Tweed, 2013; Narama and others, 2017). Once formed, ponds expand via enhanced ablation and calving (Sakai and others, 2000, 2009; Benn and others, 2001; Miles and others, 2016, 2017b) and positive feedbacks develop: increased ablation enhances surface lowering, which reduces the ice surface gradient and

© The Author(s), 2024. Published by Cambridge University Press on behalf of International Glaciological Society. This is an Open Access article, distributed under the terms of the Creative Commons Attribution licence (<http://creativecommons.org/licenses/by/4.0/>), which permits unrestricted re-use, distribution and reproduction, provided the original article is properly cited.

cambridge.org/jog



promotes further ponding (Benn and others, 2012; Watson and others, 2016; Narama and others, 2017). These positive feedbacks can increase the size and number of ponds, which may coalesce to form large proglacial lakes (Richardson and Reynolds, 2000; Miles and others, 2016; Watson and others, 2016). Supraglacial ponds can also drain on seasonal to interannual timescales, when they intersect with the englacial hydrological system and/or overtop (Benn and others, 2001; Wessels and others, 2002; Miles and others, 2017a; Taylor and others, 2022). Ice surface slope is the primary control on supraglacial pond distribution and characteristics: shallower slopes promote widespread ponding, coalescence and lake formation, whereas steeper slopes lead to more isolated ponds (Reynolds, 2000). Ice velocities also influence pond size and distribution, as faster flow encourages fractures to open, leading to pond drainage and hence limiting pond expansion and persistence (Salerno and others, 2012; Miles and others, 2016, 2017b).

Previous work attributes 11% (72 total) of GLOFs recorded in the HMA between 1833 and 2022 with an identifiable cause to supraglacial lake drainage events, compared to 49% (330 total) from moraine dammed lakes and 32% (234 total) from ice dammed (Shrestha and others, 2023). However, recurring GLOFs were often supraglacial in origin and almost all casualties were associated with failure of supraglacial or moraine dammed lakes, with the former accounting for 101 deaths from 72 recorded incidents (Shrestha and others, 2023). Furthermore, at least four of the 24 historical GLOFs observed in Bhutan originated from supraglacial lakes (Komori and others, 2012). Jointly with Nepal, Bhutan is the most vulnerable country globally to GLOFs (Liu and others, 2015; Watson and others, 2016, 2017; Miles and others, 2017a), as its glaciers are shrinking rapidly (RGoB, 2011; Carrivick and Tweed, 2016) and its proglacial lakes are expanding (Brun and

others, 2017; Maurer and others, 2019b; Shean and others, 2020). Furthermore, its main population centres, agricultural land, cultural and administrative centres lay downstream of large, rapidly growing lakes (Dorji and others, 2016). Bhutan also relies on Hydroelectric Power (HEP) to generate 100% of its power and ~45% of its GDP (UNDP Bhutan, 2011), while subsistence agriculture employs ~79% of its population (Dorji and others, 2016).

To date, most work on GLOFs in Bhutan has focused on the Lunana region, which has numerous large, growing glacial lakes that have generated multiple historical GLOFs (e.g. Richardson and Reynolds, 2000; Fujita and others, 2008; Narama and others, 2017; Maurer and others, 2020; Rinzin and others, 2023). However, prior work has highlighted the nearby Tshojo Glacier as potentially dangerous (Fig. 1): in 2009, a previously undetected ice surface pond burst and caused the downstream city of Punakha to be evacuated, although no damage was recorded (Komori and Tshering, 2010; Komori and others, 2012; Yamanokuchi and others, 2011). Tshojo Glacier is located on the southern side of the main Himalayan ridge in the Lunana region and flows southwards ($28^{\circ}6'21''\text{N}$, $90^{\circ}9'52''\text{E}$; Fig. 1). Tshojo Glacier's tongue has extensive debris cover and is situated between ~4000 and 4500 m a.s.l (Fig. 1), while the glacier as a whole is ~15 km long, making it one of the largest glaciers in Bhutan (Komori and others, 2012). Meltwater from Tshojo Glacier is main source of the Gotey chhu, one of main tributaries of Phochu River, and the glacier is located ~2.5 km upstream of the Lunana Gewog centre, which is the administrative centre for the Lunana region. There are two major hydropower plants located downstream of Tshojo Glacier: the Basochhu power plants I (capacity = 24 MW) and II (capacity = 40 MW) are located approximately 95 km downstream and the Punatsangchhu-I (capacity = 1200 MW) and Punatsangchhu-II (capacity = 1020 MW)

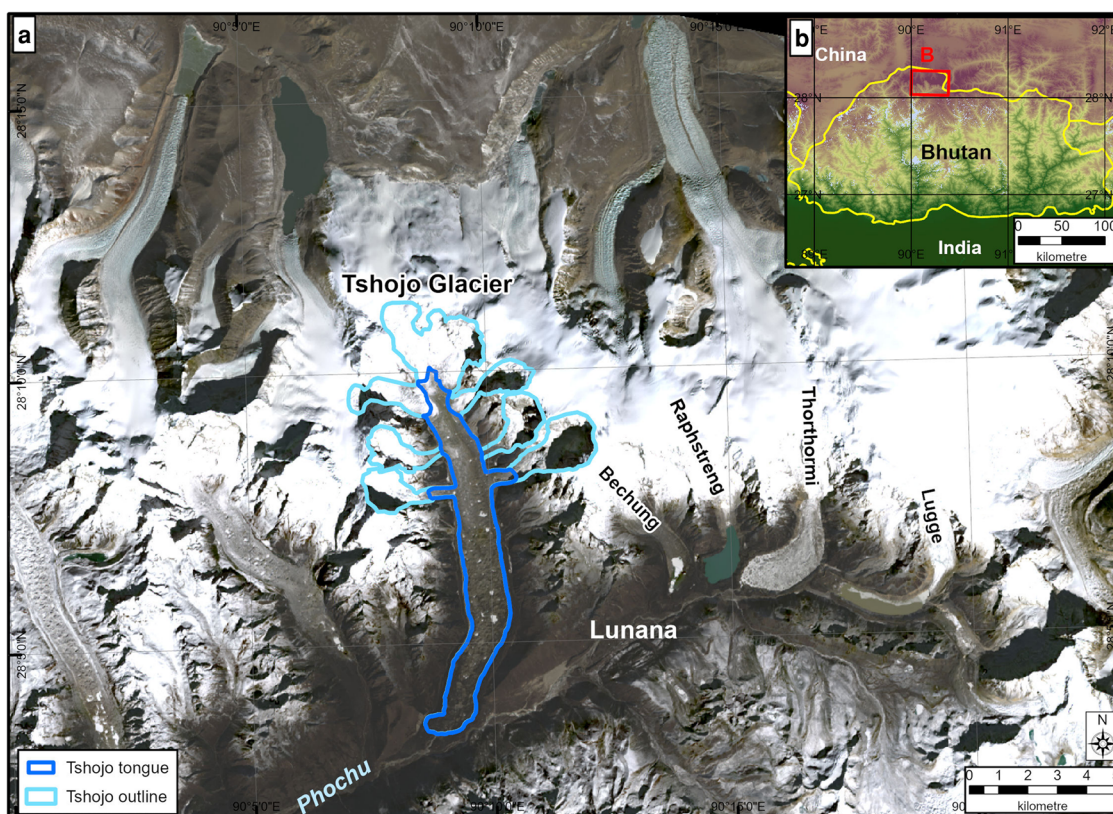


Figure 1. (a) Overview map, showing the location of Tshojo Glacier within Bhutan and the surrounding region of the Himalaya. Inset imagery is from the SRTM DEM and is colour coded by elevation. Country boundaries are indicated in yellow and the red box indicates the extent of 'b'. (b) location of Tshojo Glacier in relation to the Lunana area and other major glaciers and proglacial lakes. The glacier outline is indicated in light blue and the glacier tongue in dark blue. Both outlines were manually digitised from the background image, which is from Landsat 8, acquired on 16th Dec 2019, from USGS Earth Explorer.

plants, located ~85 km downstream. Thus, there is a pressing need to quantify the variability in water volumes stored in Tshojo Glacier's ice surface ponds, given its location directly upstream major settlements, cultural heritage sites and HEP plants. In this study, we aim to: (i) quantify the multi-decadal evolution and interannual variability of supraglacial water storage on Tshojo Glacier between 1987 and 2020; (ii) to determine controls on observed supraglacial water storage patterns, including ice velocities, longitudinal gradient of the glacier surface and air temperatures; and (iii) determine the area and infrastructure downstream that would be inundated for different pond drainage scenarios.

2. Methods

2.1. Imagery sources

We used multiple image sources to quantify multidecadal patterns in supraglacial pond volumes and locations on Tshojo Glacier. For each time period, we used the highest resolution data that were consistently available and ensured overlap between datasets to evaluate the impacts of image resolution on pond statistics. Specifically, for the period 2017–2020, we used 4-band PlanetScope scenes at 3 m resolution and for 2012–2017 we used RapidEye Ortho tiles (corrected for surface reflectance) at 5 m resolution (Table S1). Between 1987 and 2020, we utilised imagery from the Landsat Collection 2 Level-1 data, provided by the USGS Earth Explorer, specifically Landsat 4–5 TM, Landsat 7 ETM+, and Landsat 8 OLI (Table S1). To extend the data further back in time (1962–1976) we used declassified spy satellite data supplied by USGS Earth Explorer, specifically the Corona KH-4 imagery and Hexagon KH-9 Lower Resolution Mapping and 70 mm Panoramic film datasets (Table S1). Unfortunately, georeferencing could not be conducted accurately enough to reliably quantify pond areas, due to both the lack of camera information for the Corona imagery and the changes on the steep slopes surrounding Tshojo Glacier in recent decades that would otherwise be used for tie points (e.g. ridge edges). Consequently, the spy satellite imagery was used only to determine the longevity of Tshojo Glacier's large ponds and not to calculate pond area.

To improve comparability between the datasets of different spatial resolution, and because errors in pond area scale inversely with pond area i.e. errors are proportionally higher for smaller ponds (Salerno and others, 2012; Watson and others, 2016; Taylor and others, 2022), we exclude ponds less than 1000 m² in area. This threshold was chosen to minimise differences associated with image resolution, while including as much of the ponded area as possible, specifically 73% of the total ponded area for RapidEye, 81% for Planet Scope and 90% for Landsat. We evaluated differences in pond statistics (Table S2) and the spatial distribution of ponds (Fig. S2) for Planet Scope (3 m resolution) and RapidEye (5 m resolution) data using images from the same date (13 December 2017), to determine comparability between these commonly used sensors.

To minimise fluctuations in pond area due to seasonal cycles, we aimed to select images in early to mid-December (Table S1 & Fig. S1). This date was chosen to avoid monsoon cloud cover (May – August) and heavy winter snowfall (January – March), which can obscure frozen ponds. Previous work from nearby glaciers (Taylor and others, 2022) has demonstrated that maximum ponded area occurs in either winter or during the monsoon. Furthermore, Taylor and others, 2022 showed that pond drainage events occurred more frequently during the monsoon (average: 8 times/month) than the winter (average: 3 times/month), although cloud cover during the monsoon adds uncertainty to these seasonal patterns (Taylor and others, 2022). Thus, the limited data available on seasonal variations in pond area in Bhutan suggest that ponds are likely to be comparatively full and close to their

maximum seasonal extent in December. For the Planet and RapidEye imagery, all dates were in December. For Landsat 8, three image dates were in November (from 14 November onwards), for Landsat 7, one image was acquired on 26 November and three images were acquired in Nov for Landsat 4–5 (Table S1 & Fig. S1). Scenes were only used if Tshojo Glacier was fully visible and unobscured by cloud. Where required, individual scenes were mosaicked and clipped to the study area extent to generate a single image of Tshojo Glacier and its tributaries for each image date.

2.2. Quantification of pond area

To identify supraglacial ponds on Tshojo Glacier from PlanetScope imagery (2017–2020) and Landsat data (1987–2020) we used Normalised Difference Water Index (NDWI) (McFeeters, 1996). The workflow is summarised in Fig. S3. Water surfaces have high reflectance in the green band and low reflectance in the near-infrared band (Fig. S3a). NDWI uses a ratio to magnify this difference in reflectance to identify water from other surface types (i.e. ponds from supraglacial debris cover) by calculating $\frac{\Delta \text{Reflectance}}{\sum \text{Reflectance}}$ (Lillesand, 2008; Bolch and others, 2011; Jha and Khare, 2017; Miles and others, 2017a), as follows:

$$NDWI_{Green} = \frac{(Green - NIR)}{(Green + NIR)} \quad (1)$$

For the PlanetScope images we used Band 2 (Green: 0.50–0.59 μm) and Band 4 (Near-Infrared [NIR]: 0.78–0.86 μm; Table S1). The same bands were used for Landsat TM 4–5 (Band 2: 0.52–0.60 μm; Band 4: 0.76–0.90 μm) and Landsat ETM+ 7 (Band 2: 0.52–0.60 μm; Band 4: 0.77–0.90 μm; Table S1). For the Landsat 8 data, we utilised Bands 3 and 5, which equate to the Green and Near-Infrared bands, at wavelengths of 0.525–0.600 μm and 0.845–0.885 μm respectively (Table S1).

After calculating the NDWI (Fig. S3b), a threshold of water bodies vs nonwater needs to be set. Here, we made an initial estimate of the NDWI threshold by determining the NDWI value of ponds that were clearly identifiable in each image. Following previous studies (i.e. Bolch and others, 2011; Miles and others, 2017a), the initial threshold was then adjusted manually for each image, to find the optimum NDWI threshold that most accurately identified ponds while minimising misclassification errors (e.g. exposed ice cliffs and crevasses incorrectly classified as water). A final threshold of 0.07 was applied to all PlanetScope NDWI raster outputs to produce classified maps of ponds vs no ponds (Fig. S3c), and areas with NDWI values > 0.07 were exported to create polygons for each individual pond (Fig. S3e). For the Landsat data, the most appropriate NDWI threshold varied between Landsat satellites and between images, and so the threshold used for each image is provided in Table S1. Initially, we used NDWI to classify the RapidEye imagery, but the results were poor when manually compared with the imagery, and so the ponds were manually digitised. To estimate uncertainties due to the NDWI classification, we compared our PlanetScope and Landsat derived NDWI results to the manually digitised Rapid Eye data. Specifically, we compared the total ponded area obtained for an individual image date (13 December 2017), for the PlanetScope NDWI results (205 605 m²) and the manually digitised RapidEye data (206 160 m²), which resulted in a percentage difference of 0.27%. We then compared total ponded area from the Landsat NDWI classification from 10th December 2017 (155 583 m²) with all ponds from the manually digitised RapidEye data that intersected with the Landsat ponds (171 900 m²): this was necessary to facilitate direct

comparison because the coarser resolution of Landsat means that only larger ponds are detected. The percentage difference in total ponded area between the manually-digitised data and the Landsat NDWI was 10.5%.

2.3. Ice velocities, longitudinal gradient of the glacier surface and thinning rates

Ice surface velocities were determined from the Inter-Mission Time Series of Land Ice Velocity and Elevation (ITS_LIVE) project (Gardner and others, 2018), provided publicly as part of NASA's MEaSUREs 2017 program. The data provide regional-scale maps of annual ice velocities for the world's major glaciated regions, and we use the HMA data product. Velocity maps were produced annually, from 1985 to 2021, and we used data from 1988 to 2020: the first three years of data (1985–1987) had large coverage gaps over Tshojo Glacier and 2020 corresponded to our most recent pond data. In our study, we utilised individual data years, which had a spatial resolution of 240 m, and the 120 m resolution composite, which provides the average velocity across all years.

The longitudinal gradient of the glacier surface was calculated from the HMA 8-metre DEM Mosaics Derived from Optical Imagery, Version 1 (Shean, 2017). The dataset was generated from very high-resolution satellite imagery (GEO-EYE, QUICKBIRD and the WORLDVIEW satellites) and has a final spatial resolution of 8 m. The dataset was clipped to Tshojo Glacier's outline, which was determined manually from PlanetScope imagery. Following approaches developed in (Quincey and others, 2007; Miles and others, 2017a), we calculated the longitudinal gradient of the glacier surface, as opposed to surface slope, to remove the impacts of the hummocky topography often found on debris covered glaciers (i.e. undulations at the scale of tens – hundreds m). Specifically, we calculated the longitudinal surface gradient as the angle from horizontal of each point on Tshojo Glacier's surface, relative to a base contour (Fig. S4). The base contour (4060 m) was selected as the first ice surface contour up glacier from the terminus that traversed the entire glacier tongue (Fig. S4). We first calculated the vertical distance, or difference in elevation, between the base contour and all points on the glacier surface, by subtracting 4060 m from the HMA DEM data (Fig. S4A). We then determined the horizontal distance of all points on the glacier from the base contour by calculating the Euclidean distance. Next, we calculated the longitudinal surface gradient in degrees using:

$$\text{Slope } (\theta) = \tan^{-1}(\text{vertical distance/horizontal distance}) \quad (2)$$

The longitudinal surface gradient data was divided into four categories, which are associated with differing pond characteristics on Bhutanese glaciers, as defined by Reynolds (2000).

Ice surface thinning rates were determined from the HMA Gridded Glacier Thickness Change from Multi-Sensor DEMs, Version 1 (Maurer and others, 2019a). The dataset provides thickness change mosaics for selected Himalayan glaciers for the periods 1975–2000 and 2000–2016 and has a spatial resolution of 30 m. The thickness change data were created by combining digital elevation models (DEMs) derived from HEXAGON KH-9 and ASTER DEMs. The data were clipped to the manually-digitised outline of Tshojo Glacier. Changes in long-profile glacier thickness were calculated from Pléiades DSMs, generated using the Ames Stereo Pipeline (Beyer and others, 2018) and made available via the Pléiades Glacier Observatory (Berthier and others, 2024). DSMs were available for Tshojo Glacier from 7 November 2017 and 19 October 2022. We utilised the 20 m resolution product to extract long profiles, to remove small-scale undulations on the glacier surface, although visual comparison of the 2 and 20 m products showed a very similar overall profile.

We used the product generated using the Semi-Global Matching (SGM) correlator (Hirschmuller, 2007), as it is able to highly-resolve topography and minimises data gaps; no areas of noise were apparent upon visual inspection of the data (Berthier and others, 2024). Ice surface elevations were extracted along the glacier centreline from the 2017 and 2022 DSMs, at an interval of 20 m, to correspond with the data resolution.

2.4. Pond outburst flood scenarios

To determine the downstream impact from potential future scenarios of outbursts from Tshojo Glacier's supraglacial ponds, HEC-RAS 2D model (v6.4.1) with 2D shallow water equation was used to perform unsteady flow routing of 11 pond outburst scenarios from Tshojo Glacier (CEIWR-HEC, 2021). The scenarios were based on the range of individual pond areas observed during the study period, from 10 000 to 100 000 m², with an increment of 10 000 m², which corresponds to our smallest (scen1) to largest magnitude scenarios (scen10; Table 1). Detailed data from the 2009 event demonstrated full pond drainage occurred suddenly (Komori and Tshering, 2010; Komori and others, 2012; Yamanokuchi and others, 2011), meaning that Scenarios 1 to 10 could occur approximately annually, depending on the exact cycle of the largest ponds. We also include a worst-case scenario: this uses the total area of all ponds visible on the 2008 image, which was the largest total ponded area observed on Tshojo Glacier during the study period. It represents the 'worst-case' scenario, whereby ponded area is at its observed maximum and all ponds drain at once, which represents an unlikely, but plausible, end-member scenario potentially triggered by a rare event, such as a catastrophic mass movement event, as observed in Chamoli (Shugar and others, 2021) and/or sudden release of water following blocking of a subglacial conduit, as observed on the Changri Shar and Khumbu glaciers (Miles and others, 2018). For each scenario, we used a different flow hydrograph, which is the function of pond volume for that scenario as an upstream boundary condition, while keeping other parameters constant (Table 2). To estimate pond volumes from observed pond areas, we applied an empirical area-volume relationship that was developed based on data from supraglacial ponds on debris-covered glaciers in the Himalaya (Watson and others, 2016). For the worst-case scenario, we converted the area of each pond detect to volume using the same empirical equation and then summed the estimated volumes to get a total volume for 2008. Specifically:

$$V = 0.1535 * A^{1.39}$$

Table 1. Area of supraglacial pond and corresponding empirically derived flood volume and peak discharge (Qp) calculated from Eqn (4) for each scenario considered in the study and then inputted into the HEC-RAS 2-D hydrodynamic model.

Scenario	Area 10 ³ m ²	Volume 10 ⁶ m ³	Qp m ³ s ⁻¹
scen1	10	0.06	10.84
scen2	20	0.15	20.67
scen3	30	0.26	30.15
scen4	40	0.38	39.41
scen5	50	0.52	48.52
scen6	60	0.67	57.50
scen7	70	0.83	66.37
scen8	80	1.00	75.16
scen9	90	1.18	83.88
scen10	100	1.37	92.52
Worst-case	350	7.80	297.13

Table 2. Amount of agricultural land, footpaths, buildings and bridges exposed to our range of scenarios of supraglacial pond outburst flood from Tshojo Glacier. Pond area and volume for each scenario are given in Table 1.

Scenario	Agricultural land m ²	Footpath km	Buildings	Bridges
scen1	1422	0.4	0	2
scen2	1512	1.0	0	2
scen3	1512	1.1	0	2
scen4	1512	1.2	0	2
scen5	1512	1.3	0	2
scen6	1512	1.3	0	2
scen7	1512	1.3	0	2
scen8	1512	1.3	0	2
scen9	1512	1.4	0	2
scen10	1512	1.4	0	2
Worst-case	44 930	1.8	13	3

where:

$$V = \text{Pond volume (m}^3\text{)} = \text{Pond area (m}^2\text{)} \quad (3)$$

Based on observations of previous supraglacial pond drainage on Tshojo Glacier (Yamanokuchi and others, 2011), and in the neighbouring central Himaya (Kropáček and others, 2015), we assumed that each pond drains fully in each scenario. Thus, the estimates presented are upper bounds for potential flood volume and resultant downstream extent.

2.5. Pond outburst model parameters

The model domain was established by creating a 500 m buffer zone on both sides of the centreline of the Phochu River, downstream of Tshojo Glacier's terminus (Fig. 1). Within this model domain, a computational mesh with a grid resolution of 30 × 30 m was generated. ALOS-PALSAR DEM, which is a SRTM 30 GL1 resampled to a ground resolution of 12.5 m, was used to derive the terrain information for the model setup. The DEM data was hydrologically corrected by filling the sinks and burning the artificial channel in the areas where deep gorges are detected as sinks, as per the approach used by Rinzin and others (2023). The HMA 8-metre DEM used to determine Tshojo Glacier's longitudinal surface gradient could not be used for the GLOF modelling across the entire domain, as its coverage is limited and patchy. However, HMA DEM data were available within ~10 km of Tshojo Glacier's snout and we therefore used this smaller domain to evaluate the sensitivity of our results to DEM resolution. Specifically, we ran Scenario 10 (i.e. pond area = 100 000 m²) with both the ALOS-PALSAR DEM and HMA 8 m DEM and compared their resulting flow hydrodynamics.

The other essential model input parameters are boundary conditions and the Manning's roughness coefficient n . The inflow hydrograph was imposed as upstream boundary condition, while the downstream boundary condition at the outlet was assumed normal depth (i.e. average slope at the downstream boundary condition) with the discret energy slope of 0.01/The latter was determined by taking the bed slope across a profile length of 500 m, perpendicular to the downstream boundary condition. The supraglacial pond volume calculated using Eqn (3) was used as the total flood volume for the inflow hydrograph construction (Table 2). The initial condition for the 2D flow area was established by setting 2D initial condition ramp-up time of 10 hours out of which 10% was allocated for ramping up the 2D boundary conditions up from zero to their first value (CEIWR-HEC, 2021).

The Manning's n value represents the resistance to flow from channel and flood plain and plays an influential role in the

propagation of flow downstream and resulting flow dynamics (CEIWR-HEC, 2021). A spatially distributed pixel-based Manning's value was assigned based on land cover data from the International Centre for Integrated Mountain Development (ICIMOD) (Uddin, 2021). In certain areas, the river channel was not well resolved by the landcover map, so we manually mapped the river channel using high resolution, publicly available Google Earth imagery, which was from Pleiades Neo 4, with a date of 27 December 2023 and a horizontal resolution of 30 cm, and assigned a Manning's value of 0.035 to this manually mapped channel (Arcement and Schneider, 1989). The Manning's n values defined from the landcover dataset and Google Earth ranged between 0.02 and 0.12. Due to the potentially importance influence of this value on our results, we conducted further sensitivity analysis. As for our DEM sensitivity assessments, we utilised scenario 10 and varied the value for Manning's n between our calculated range of 0.02 and 0.12, in increments of 0.01. We then compared flood hydrodynamic data (flow arrival time and peak flow) at three sites, located at distances of 5, 10 and 20 km downstream of Tshojo Glacier respectively.

The water released from supraglacial lakes can drain either into existing sub- or englacial conduits, and eventually emerges at the glacier snout (Richardson and Reynolds, 2000), or can flow supraglacially, if it overwhelms the sub- and englacial drainage networks (Miles and others, 2018). The exact routing depends on a variety of factors, including the glacier geometry near the terminus and the configuration of the drainage network, which are very difficult to quantify in the absence of directly measured data. Thus, we assumed the worst case scenario (i.e. the most rapid water delivery to the snout) and calculated peak discharge using the empirical equation of tunnel drainage events proposed by Clague and Mathews (2017) (Eqn (4)). Due to the difficulties involved in collecting essential parameters such as drainage tunnel size, temperature or filling level of the lake, using a numerical approach to generate the flow hydrograph was not possible (Kropáček and others, 2015). Instead, we estimated the hydrograph by fitting the peak flow and volume of each scenario to a log-normal distribution curve with a sigma value of 4.5 and mean of 1 following the convention used by (Kropáček and others, 2015).

$$[Q_{\max}] = 75 V_{\max}^{0.67}$$

where:

$$\text{Where } Q_{\max} = \text{peak discharge } V_{\max} = \text{maximum volume.} \quad (4)$$

2.6. Pond outburst impact assessment

To estimate the extent of flood inundation downstream caused by an outburst from Tshojo Glacier's supraglacial ponds, we collated flow depth from all scenarios and assigned a consistent value of 1. The final flood inundation map was produced by summing the resulting inundation extents from all 11 scenarios. This map depicted the range of pixel values from 1 to 11, corresponding to the number of scenarios that affected a specific area. For instance, a pixel with a value of 1 indicated that the area was impacted solely from one scenario, while a pixel with a value of 11 indicated impact from all 11 scenarios.

To assess the exposure of downstream infrastructure and settlements to our modelled potential outburst floods from Tshojo Glacier, we extracted the buildings, roads, and bridges that intersect with our flood inundation maps from the OpenStreetMap. We also overlaid these data on Google Earth imagery from 27 January 2021 (i.e. the closest date to the Open Street map data)

and manually checked its accuracy. Fortunately, OpenStreetMap had good coverage of buildings and infrastructure within the inundation map, except for the two suspension bridges in the Lunana region, which we added manually. However, the existing OpenStreetMap and land-use and land cover maps at the global and Hindu Kush Himalaya (HKH) scales (Uddin, 2021; Brown and others, 2022) do not adequately resolve the agricultural land, so we manually mapped the agricultural land within our model domain using Google Earth imagery.

3. Results

3.1. Comparison of pond statistics between PlanetScope, RapidEye and Landsat imagery

We observed limited difference between for total ponded area (0.27% difference), area of the largest pond (0.76%), and percentage of the glacier tongue covered by ponds (0.54%; Table S2 & Fig. S2), and so we treat these statistics as directly comparable between the two datasets. Differences were somewhat higher for the number of ponds (7.23%) and the mean area across all ponds (6.69%; Table S2) but remained small enough to be broadly comparable. Landsat data were not available on the same dates as PlanetScope or RapidEye and so we compared images within three days of each other, to minimise any temporal variability. For PlanetScope and Landsat imagery, the total ponded area (0.94%), area of the largest pond (4.63%) and percentage of the glacier tongue covered by ponds (0.94%) were thus directly comparable (Table S3, Fig. S2). However, differences in the number of ponds (41.13%) and mean pond area (42.02%) were large, so are not directly compared in this study (Table S3). For RapidEye and Landsat data, the total ponded area (14.95%), area of the largest pond (10.63%) and percentage of the glacier tongue covered by ponds (14.95%) were broadly comparable (Table S4, Fig. S2), but the number of ponds (29.65%) and the mean pond area (40.09%) were not (Table S4). We attribute these differences in mean pond area and number of ponds for Landsat vs PlanetScope/RapidEye to the difference in image resolution: Landsat does not detect the substantial number of smaller ponds (Fig. S2), leading to a lower count and a higher mean pond size, but total ponded area is largely unaffected by resolution, as it is dominated by the larger ponds.

3.2. Temporal variability in bulk pond statistics

We used Landsat data to investigate temporal variability in total pond area, percentage of the glacier tongue covered by ponds and the area of the largest pond, because values for these variables were comparable across the different image resolutions (Tables S3 & S4) and Landsat enables us to construct the longest temporal record. Total ponded area on Tshojo Glacier showed two distinct periods during our study period: it doubled between the earlier portion (1987–2003) and the latter portion (2007–2020), increasing from 104 529 m² to 213 943 m² (Fig. 2a). Interannual variability in total ponded area also increased markedly between these two time periods: the largest change between consecutive years in the earlier period was 85 500 m², between 2001 and 2002, compared to 165 600 m² between 2012 and 2013 (Fig. 2a). Over the entire study period, total ponded area varied by approximately an order of magnitude, from 34 200 m² in 1997 to 331 200 m² in 2008 (Fig. 2a). The percentage of the glacier tongue covered by ponds was derived from total pond area, so follows the same temporal pattern, and ranges between 0.23 and 2.2% of Tshojo Glacier's area (Fig. 2b). As for total ponded area, the area of the largest pond increased markedly between 1987 and 2003 (average area = 16 457 m²) and 2007–2020 (average area = 60 879 m²;

Fig. 2c). Likewise, the interannual variability increased by an order of magnitude between these two time intervals, with the largest year-on-year change during the earlier period being 8100 m² (1997–1998), compared to 83 700 m² during the later period (2014–2015; Fig. 2c). Finally, we observed no apparent up-glacier migration in pond locations of any size at multi-decadal time scales (Fig. S5).

To assess variability in the number of ponds and mean pond area for ponds above the 1000 m² threshold, we use data obtained from PlanetScope and RapidEye, as these variables are sensitive to image resolution (Tables S3 & S4) and so the highest image resolution available was used. Between 2012 and 2020, the number of ponds showed a net reduction over time (Fig. 3a). The number of ponds showed considerable interannual variability between 2012 and 2017, ranging between 51 in 2013 and 35 in 2017 (Fig. 3a). Pond number was lowest in 2020, at 30 ponds (Fig. 3a). Mean pond area increased overall between 2012 and 2020 (Fig. 3b) but was temporarily variable: mean pond area increased from 2837 m² in 2012 to 5256 m² in 2015, before decreasing to 3727 m² in 2016. Thereafter, mean pond area increased again to 5230 m² in 2018 and remained at similar values until the end of the dataset in 2020 (Fig. 3b).

3.3. Temporal variability in large ponds

Our data demonstrate that both the number and area of large ponds increased dramatically between 1987–2003 and 2007–2020 (Fig. 4). Specifically, from 2007 onwards, we observed seven ponds over 50 000 m², two between 500 000 and 40 000 m² and nine between 40 000 and 30 000 m², whereas no ponds were found in these categories between 1987 and 2003 (Fig. 4). Furthermore, ponds with an area between 20 000 and 30 000 m² increased from four in 1987–2003 to 16 in 2007–2020 and those between 10 000 and 20 000 m² increased from 21 to 29 for the same time intervals (Fig. 4). Finally, the number of ponds between 1000 and 10 000 m² increased from 248 to 343 (Fig. 4).

Focusing on individual ponds, the largest (117 000 m² in 2008) and the second largest (116 100 m² in 2015) individual pond area observed during the time series occurred when Pond B and D merged and the third largest was Pond A, reaching 100 800 m² in 2013 (Fig. 4; Table S5). The area of an individual pond exceeded 50 000 m² at three different ponds during period: three times at BD, twice at A and once at V (Fig. 4; Table S5). Pond A reached over 40 000 m² twice during the study period, while the ponds exceeding 30 000 m² were: B three times, A and V twice, and C and H once (Fig. 4; Table S5). Ponds that exceeded over 20 000 m² during the study period were: A five times, Y four times, J twice and Ponds B–F, H, M, S and V once (Fig. 4; Table S5). Thus, our data indicate that the largest ponds consistently form at the same locations during our study period. This is supported by data from the declassified satellite imagery, in which we identified most of our large ponds (A, B, D, F, H, M, V and Y) in images from 1967, 1974 and 1976 (Fig. S6). This demonstrates that some of the large ponds have formed in the same location on Tshojo Glacier for at least 53 years. Of the ponds over 20 000 m² (Fig. 1), we did not observe ponds C, E, J or S in the declassified imagery (Fig. S6). We could not definitively identify any ponds in declassified imagery from 1966 or 1962 (Fig. S6).

3.4. Ice velocities, longitudinal gradient of the glacier surface and thickness change

Overall, Tshojo Glacier's ice velocities increased with distance from the terminus and the glacier margins (Fig. 6a). Velocities were low (≤ 5 m a⁻¹) over the lowest 4.5 km of the glacier tongue

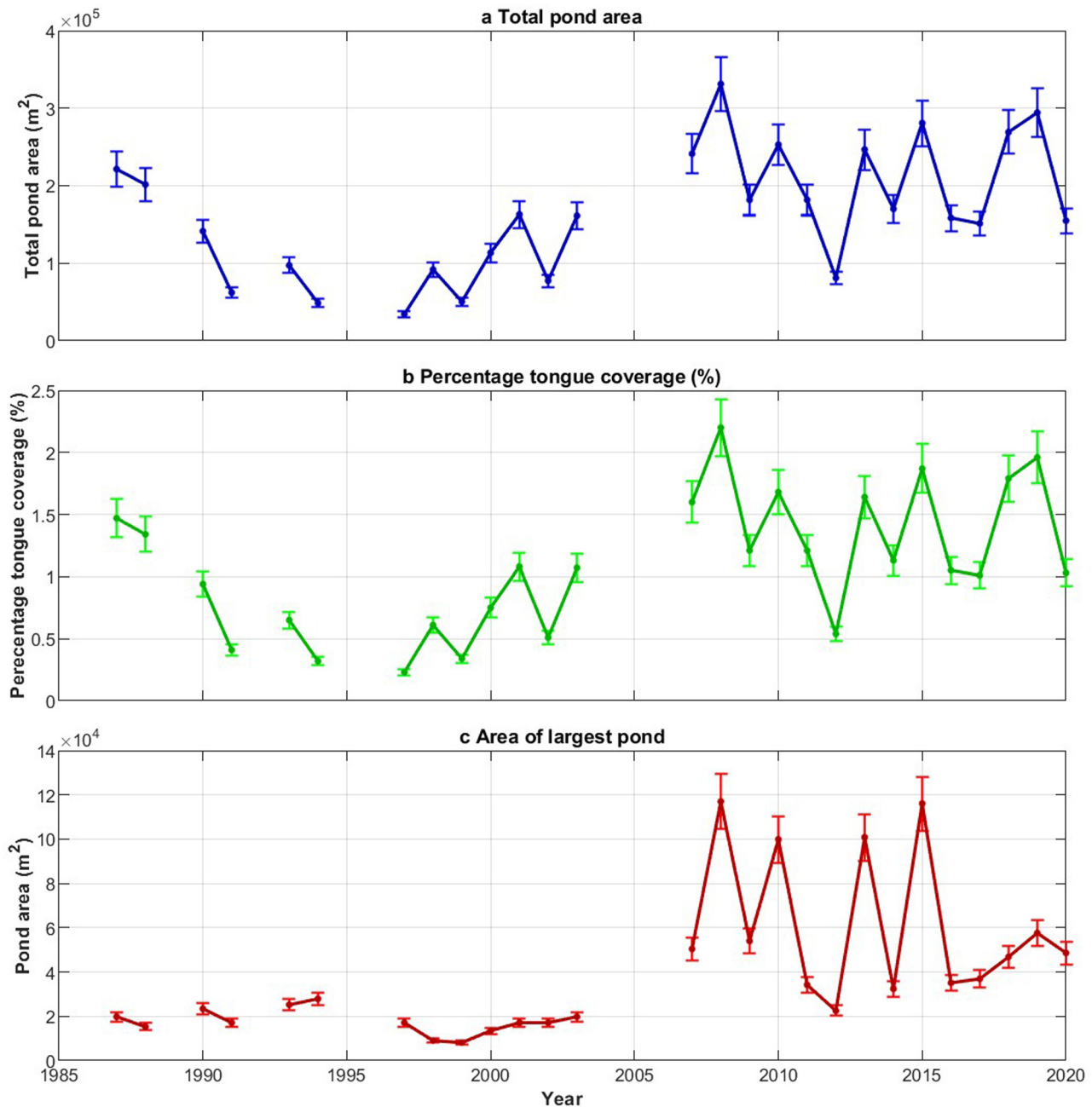


Figure 2. Variability in (a) Total area of all ponds on Tshojo Glacier; (b) the percentage of Tshojo Glacier's tongue covered by ponds; and (c) the area of the largest pond detected in a given year on Tshojo Glacier, for the period 1987 to 2020, derived from Landsat imagery (30 m resolution). Error bars (lighter colours) show the 10.5% error calculated for the Landsat data (Section 2.2). Values are given for ponds over 1000 m² only. Data are from Landsat 4–5 TM (1987–2003), Landsat 7 ETM+ (2007–2012) and Landsat 8 (2013–2020) and specific image dates and details are given in Table S1.

and increased to over 50 m a⁻¹ at ~12 km from the terminus (Fig. 6a & c). Tshojo Glacier slowed down between 1998 and 1993, particularly in its middle section (~4–10 km from the terminus), where ice velocities reduced by ~10 m a⁻¹ (Fig. 6c). Smaller magnitude reductions in ice velocities were also observed over the lower 4 km and the upper ~1 km of the glacier tongue (Fig. 6c). Ice velocities remained low in 2003, before increasing slightly in the middle section of the glacier tongue (~4–10 km) for the remainder of the study period (Fig. 5c).

The longitudinal surface gradient of Tshojo Glacier's tongue ranged between 0 and 6° in 2017 (Fig. 5b). The majority of the glacier was classified in the 3–6° category and about 20% of the glacier was classified as >2° (Fig. 5b). Longitudinal surface gradient did not show a clear trend with distance up glacier. However, patches of lower longitudinal surface gradient occurred along the glacier centreline line from the terminus to ~10 km up glacier

(Fig. 5b). Areas of lower longitudinal surface gradient were also apparent along the eastern margin of Tshojo Glacier's tongue, between ~5 and 11 km up glacier (Fig. 5b). Surface elevation at Tshojo Glacier showed a broadly linear increase along its centreline, from ~4000 m a.s.l. at the terminus to ~4450 m a.s.l. at the top of the glacier tongue, approximately 12 km up glacier, and was characterised by undulations of tens to hundreds of meters in amplitude (Fig. 5d).

Rates of ice thinning on Tshojo Glacier increased markedly between 1975–2000 and 2000–2016, particularly over the middle of the ice tongue (~3–10 km from the terminus; Figs 6a, b). In 1975–2000, rates of thinning on the lower 8 km of Tshojo Glacier's tongue were generally between -0.25 and -0.75 m a⁻¹, with isolated patches of higher thinning rates (between -0.75 and -1.25 m a⁻¹) and net thickening (Fig. 6a). Thinning rates were somewhat higher up glacier of 8 km, at between -0.75 and

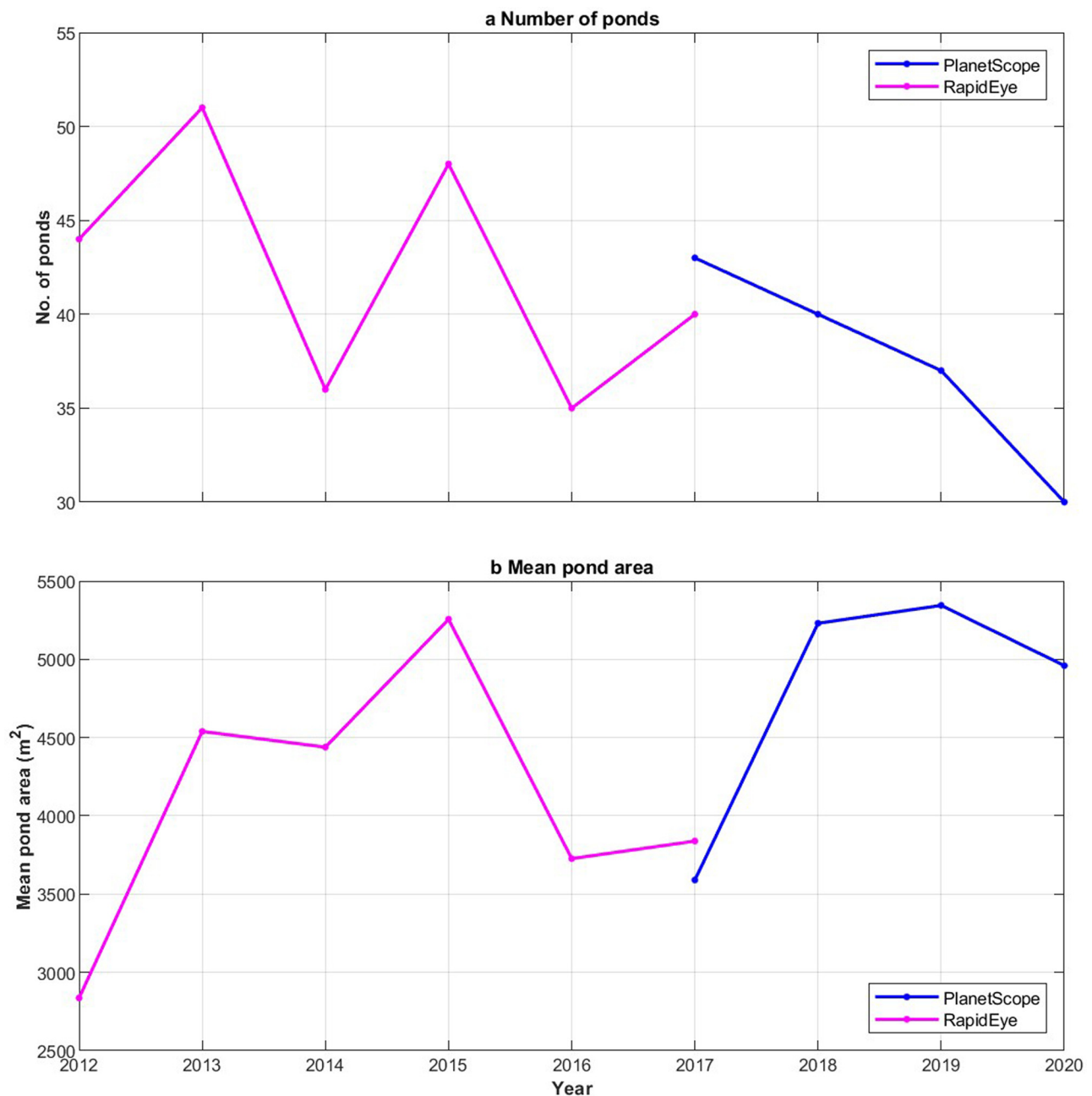


Figure 3. Variability in (a) the number of ponds and (b) mean area of the ponds on Tshojo Glacier between 2012 and 2020. Values are given for ponds over 1000 m² only. Magenta indicates data derived from RapidEye imagery (5 m spatial resolution) and dark blue indicates PlanetScope (3 m resolution). Specific image dates and details are given in Table S1. Error in the PlanetScope data, relative to our manually digitised reference ponds from RapidEye, was 0.27%.

1.25 m a⁻¹ (Fig. 6a). For 2000–2016, ice thinning rates were generally > -1 m a⁻¹ over the middle portion of the tongue (~3–10 km), with substantial patches reaching over -2 m a⁻¹, and maximum rates of thinning occurred between 3 and 8 km from the terminus (Fig. 6b). Over the lower 3 km of Tshojo Glacier's tongue, ice thinning rates for 2000–2016 were similar to 1975–2000, at -0.25 to -0.75 m a⁻¹ and rates of thinning were also comparable between the two time periods above ~10 km (Fig. 6b). For both time intervals and all areas of the glacier, the spatial pattern of ice thinning was heterogeneous and patchy (Figs 6a, b). Limited changes in glacier long profile were observed between 2017 and 2022 (Fig. 5d).

3.5. Pond outburst hydrodynamics and downstream impacts

Applying Eqn (3) to our drainage scenarios gave pond volumes of between $0.06 \times 10^6 \text{ m}^3$ (10 000 m³) and $1.37 \times 10^6 \text{ m}^3$ (100 000 m³), with a worst-case scenario of $3.03 \times 10^6 \text{ m}^3$ i.e. the total pond

volume recorded in 2008, which was the maximum observed during our study period (Table 1). In our potential breach scenarios for these ponds, the peak discharge ranged between 10.84–92.52 m³ s⁻¹ for scen1 to scen10 and was 119 m³ s⁻¹ for the 'worst-case' scenario (Table 1). Our results suggest that the downstream propagation of the flow wave varied from ~6 km (scen1) to ~35 km (scen10) and reached a maximum of 47 km in the worst-case scenario (Figs 7–9). All scenarios reached the Lunana area and, although the worst-case scenario travelled further downstream, it attenuated before reaching the next settlement at Wolathang village (Figs 7–9). In all scenarios, the flood waves arrived at Lunana within an hour of initiation at the upstream boundary, with the worst-case scenario arriving ~5 minutes earlier than the more moderate scenarios (Fig. 8). For scenarios 1–10, the flow magnitude at Lunana was similar in magnitude to the initial discharge, ranging from 5–86 m³ s⁻¹ (Figs 8a, b). The mean flow velocity ranged between 0.1–2 m s⁻¹ while the maximum velocity was up to 9 m s⁻¹ (Figs 7, 10d).

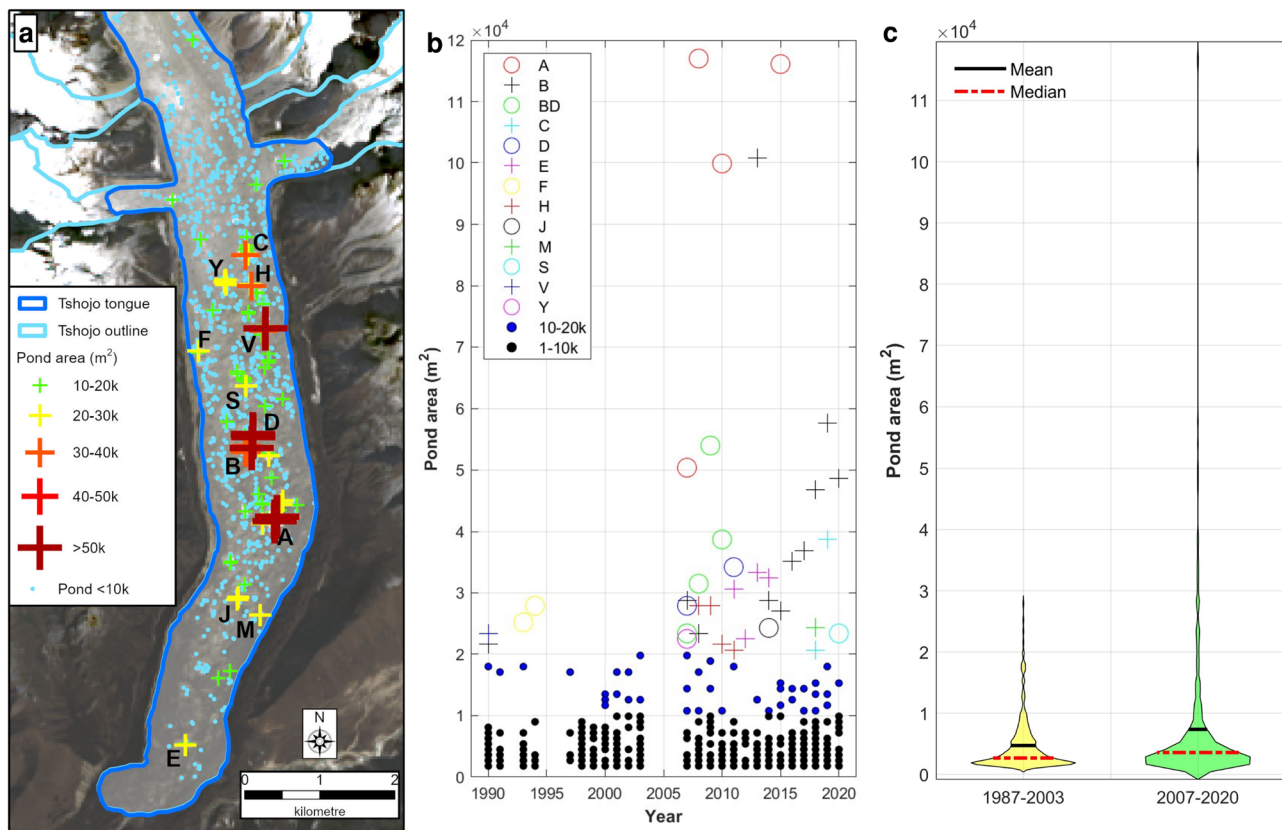


Figure 4. Location and area of large ponds detected on Tshojo Glacier between 1987 and 2020. (a) Location of ponds on Tshojo Glacier. Ponds larger than 10 000 m² are symbolised by size and colour, according to pond area category. Ponds smaller than 10 000 m² are symbolised by a cyan dot. Ponds larger than 20 000 m² are named. (b) Individual pond area by year. For ponds larger than 20 000 m², symbol type and colour indicate the pond letter, located in (a). Note that B and D indicate separate ponds and BD denotes incidences when B and D merge. Ponds smaller than 20 000 m², are symbolised with a blue dot (10 000–20 000 m²) or a black dot (less than 10 000 m²). (c) Violin plots of pond area for 1987–2003 and 2007–2020, with the mean indicated by the black line and the median by the do-dashed red line.

Meanwhile, the mean flow depth varied between 0.1–1 m, with a maximum depth of up to 10 m (Figs 7, 10e). Our inundation map shows that the outflow from all modelling scenarios was largely confined within the pre-existing flood plain (Fig. 9). An exception to this was observed in Lunana village (Fig. 9d), where approximately 90 m² of agricultural land was inundated in scenario 1 to 10 and 1410 m² was exposed in the worst-case scenario. All the scenarios intersected with the network of footpaths in Lunana, impacting between 0.3 (scenario 1) to 1.2 km (worst-case scenario) of the paths and two suspension bridges.

Focusing on our sensitivity analysis, varying the manning n value had limited effect on peak and total flow close to Tshojo Glacier but its impact increased with distance downstream. Specifically, at 5 km downstream of Tshojo Glacier, the peak flow decreased by 2% (between 94 and 93.4 m³ s⁻¹) when Manning's number was increased from 0.02 to 0.12 (Fig. S7). This peak flow decreased by 3% (between 94 and 92 m³ s⁻¹) at 10 km downstream and by 52% (between 78 and 38 m³ s⁻¹) at 20 km downstream (Fig. S7). The changes in total flow and duration exhibited a similar pattern in response to changes in the Manning's n value (Fig. S7). The flow arrival time was sensitive to the choice of Manning's n value and this sensitivity increases with distance from Tshojo Glacier (Fig. S7). For example, at a distance of 5 km downstream, every 0.1 increase in Manning's n value results in to flow delay of 3.6 minutes, totalling almost 40 minutes when Manning's n increased from 0.02 to 0.12. This delay increased to 46 minutes per 0.1 increase in Manning's n and reached a total delay of 8 hour at 20 km downstream. Furthermore, we observed a linear relationship ($R^2 = 0.9$ to 0.99) between flow arrival time and Manning's n variations,

with linearity strengthening as the distance increased from 5 km ($R^2 = 0.9$) to 20 km ($R^2 = 0.99$) downstream of Tshojo Glacier.

There was minimal variation in simulated peak and total flow from our model runs using the SRTM DEM vs the high-resolution HMA 8 m DEM (Fig. S8). Likewise, there was no substantial discrepancy in flow arrival at 5 km and 10 km downstream of Tshojo Glacier, but at 20 km downstream, flow modelled with HMA 8 m DEM arrived slightly earlier than the simulations using the SRTM DEM (Fig. S8). The inundation extent from both the DEMs remained within the flood plain in both cases (Fig. S8), although the inundation pattern from the SRTM DEM was patchier at the fine scale.

4. Discussion

4.1. Temporal patterns in pond characteristics

Overall, our data show an increase in total ponded area on Tshojo Glacier between 1987 and 2020 (Fig. 2a). This is consistent with supraglacial lake expansion observed elsewhere in the eastern Himalaya in recent decades, which has been attributed to the combined impacts of climate warming and glacier thinning (e.g. Gardelle and others, 2011; Watson and others, 2016; Nie and others, 2017; Khadka and others, 2018). We also observe large interannual variation in total ponded area on Tshojo Glacier, particularly from 2007 onwards (Fig. 2a). Similar temporal variability has been previously reported elsewhere in Bhutan (Taylor and others, 2022) and the eastern and central Himalaya (e.g. Gardelle and others, 2011; Wang and others, 2015; Watson and others, 2016; Nie and others, 2017; Steiner and others, 2019;

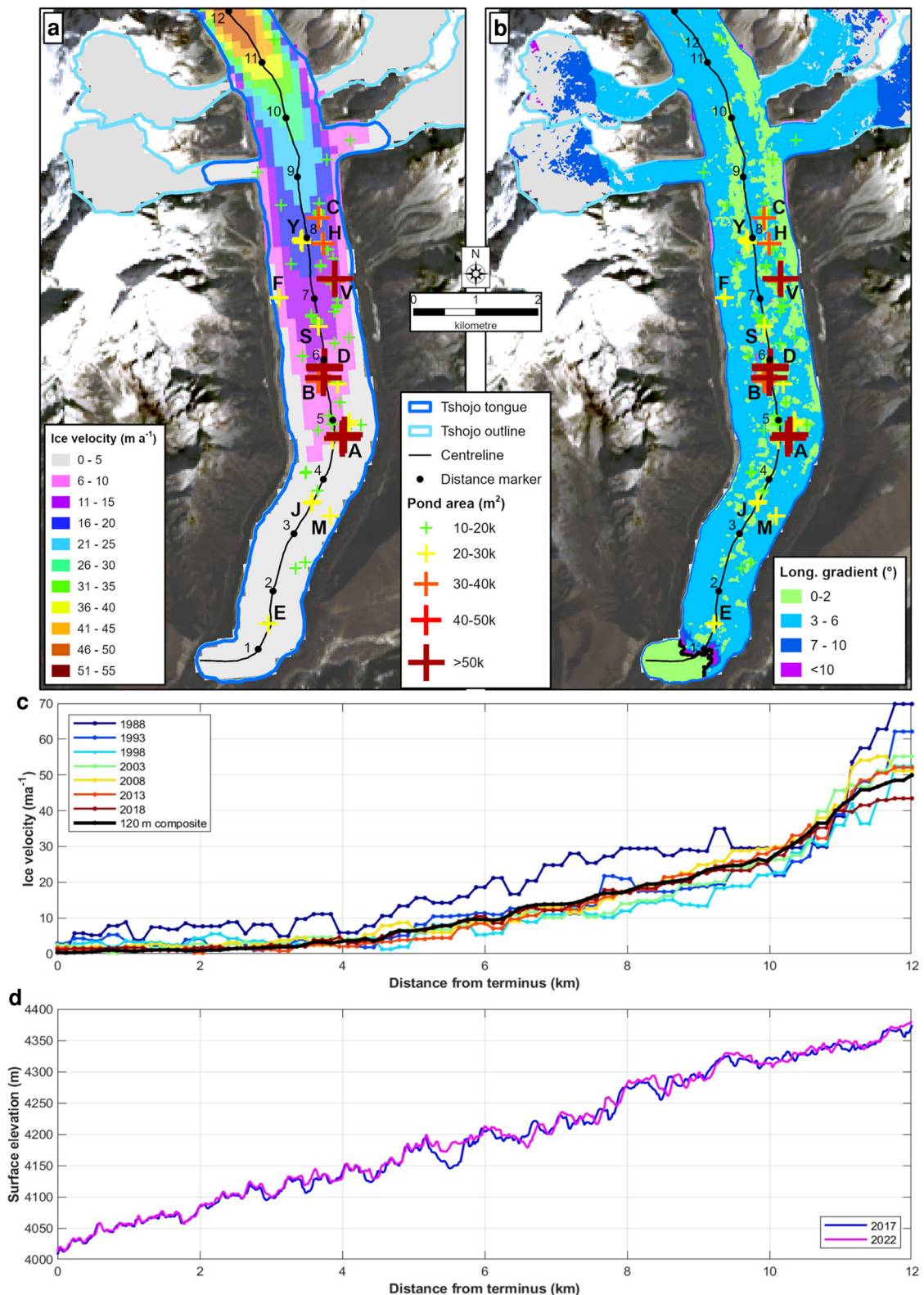


Figure 5. Ice velocities, longitudinal gradient of the glacier surface, and supraglacial pond distribution on Tshojo Glacier. (a) Map of ice velocities from ITS LIVE 120 m composite, compiled from velocity data from 1988–2020. (b) Map of the longitudinal gradient of the glacier surface, derived from High Mountain Asia 8 m resolution DEM (data date: 16 July 2017). Panels a & b show the location and area of all ponds on Tshojo Glacier detected during the study period (1987–2020). Ponds larger than 10 000 m² are categorised and symbolised by size and colour. Ponds smaller than 10 000 m² are symbolised by a cyan dot. Ponds larger than 20 000 m² are named. In panels a & b the thin black line represents the glacier centreline, with distance markers (black circle) numbered by distance in kilometres from the glacier terminus, along the centre line. In panel b, the thick black line represents the 4060 m contour, which was the baseline from which slope was calculated (See Section 2.4). (c) Centreline ice velocities from selected years. Velocities were sampled every 120 m along the centreline (black line) shown in a. Lines are colour coded by year and displayed every 4 years from 1988. The black line shows the velocity profile from the 120 m composite. (d) Centreline surface elevation profiles, sampled every 20 m from Pléiades DSMs from 7 November 2017 (blue line) and 19th October 2022 (magenta line). The DSMs were provided by the Pléiades Glacier Observatory (Berthier and others, 2024).

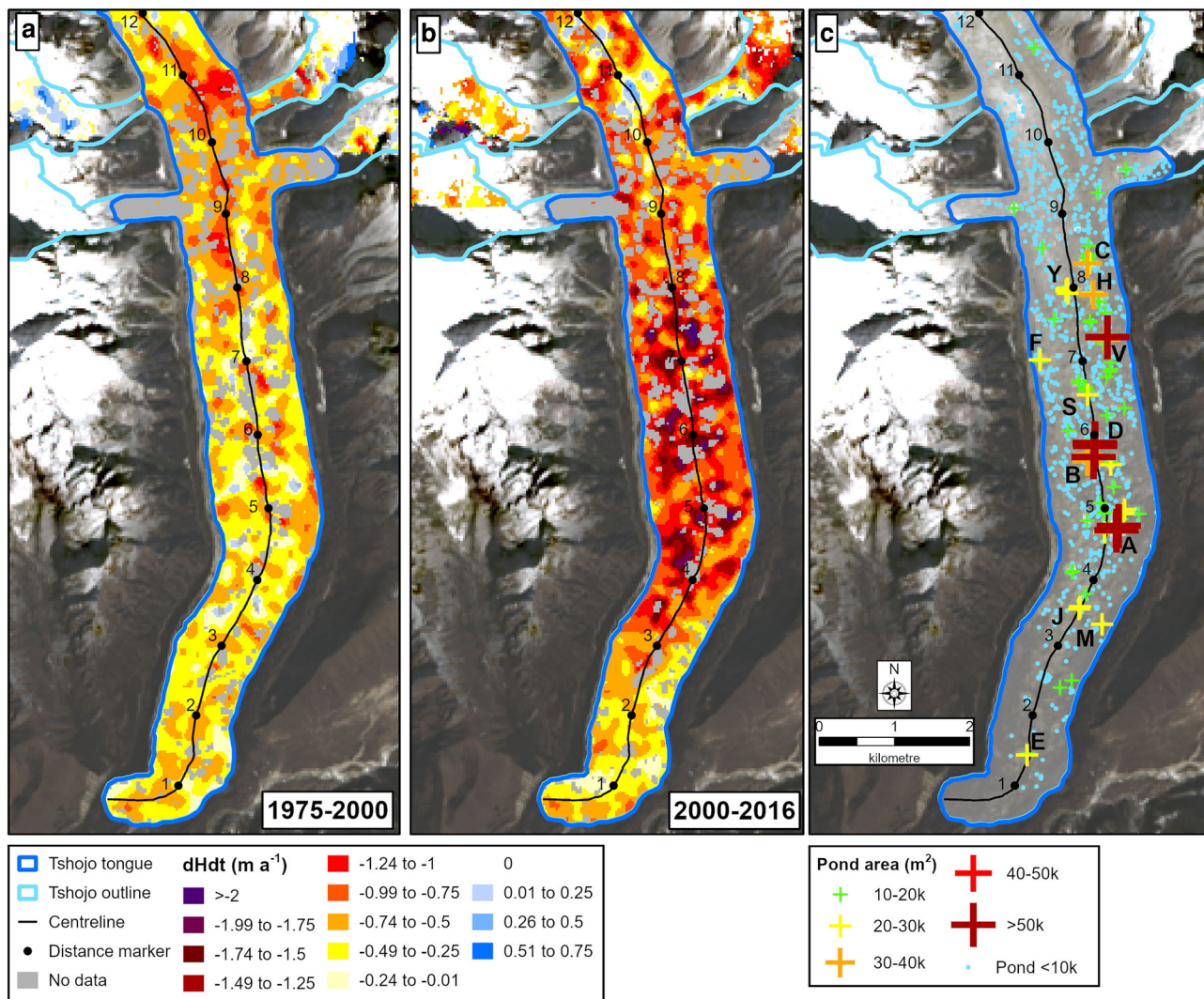


Figure 6. Map showing ice thickness change and its correspondence with supraglacial pond distribution on Tshojo Glacier, for (a) 1975–2000 and (b) 2000–2016. Ice thickness change is derived from the High Mountain Asia Gridded Glacier Thickness Change from Multi-Sensor DEMs, Version 1 (Maurer and others, 2019a). Gaps in the ice thickness change data are symbolised in mid-grey. (c) Location and area of all ponds on Tshojo Glacier detected during the study period (1987–2020). Ponds larger than 10 000 m² are categorised and symbolised by size and colour. Ponds smaller than 10 000 m² are symbolised by a cyan dot. Ponds larger than 20 000 m² are named.

Kneib and others, 2021), suggesting that the temporal evolution of ponded area on Tshojo mirrors the regional pattern of large inter-annual variability, within an overall trend of decadal-scale pond expansion.

Our data show that interannual variations in ponded area and the percentage of the glacier tongue covered by ponds were predominantly driven by changes in the area of the largest ponds (Figs 2c, 4) and that these large ponds occupied similar locations throughout the study period (Fig. 4). This is supported by declassified spy satellite imagery (Fig. S6), which showed that most of Tshojo Glacier's major ponds occurred at the same locations for at least 53 years. This duration of consistent pond locations is among the longest reported for the Himalaya, with previous work demonstrating pond recurrence over ~10-year time intervals in the Everest and Langtang region (Watson and others, 2016; Steiner and others, 2019), reaching up to 28 years at the termini of large Everest glaciers (Chand and Watanabe, 2019). We suggest that ponds repeatedly formed at the same locations on Tshojo Glacier initially due to local ice characteristics (e.g. basal topography, surface geometry and uneven melt) and are then maintained via a series of melt-related feedbacks, as observed elsewhere in the Himalaya (e.g. Benn and others, 2012; Watson and others, 2016). Furthermore, the regular drainage events observed

on Tshojo Glacier may also aid pond persistence and the growth of the largest ponds: data from Ngozumpa Glacier, Nepal, suggest that englacial pond drainage may remove debris, causing localised enhancement of melt rates, and prevent ponds from overflowing, thus encouraging higher melt rates and incision at the pond margins (Strickland and others, 2023).

4.2. Controls on pond location and characteristics

On debris-covered glaciers, surface slope is the primary control on the location and characteristics of supraglacial ponds (e.g. Reynolds, 2000; Quincey and others, 2007; Sakai and Fujita, 2010; Salerno and others, 2012; Miles and others, 2017a; Miles and others, 2020). Specifically, longitudinal surface gradients of less than 2° promote the formation of large ponds and encourage individual ponds to merge, while those between 2 and 6° are usually associated with the formation of individual ponds, which are transient and cover substantial areas of the ice surface (Reynolds, 2000). The majority Tshojo Glacier has a longitudinal surface gradient of between 2 and 6° (Fig. 5b), which we suggest is sufficiently flat to encourage widespread pond formation and growth, but too steep for large, linked ponds to form and persist. Furthermore, approximately 20% of Tshojo Glacier's surface has a

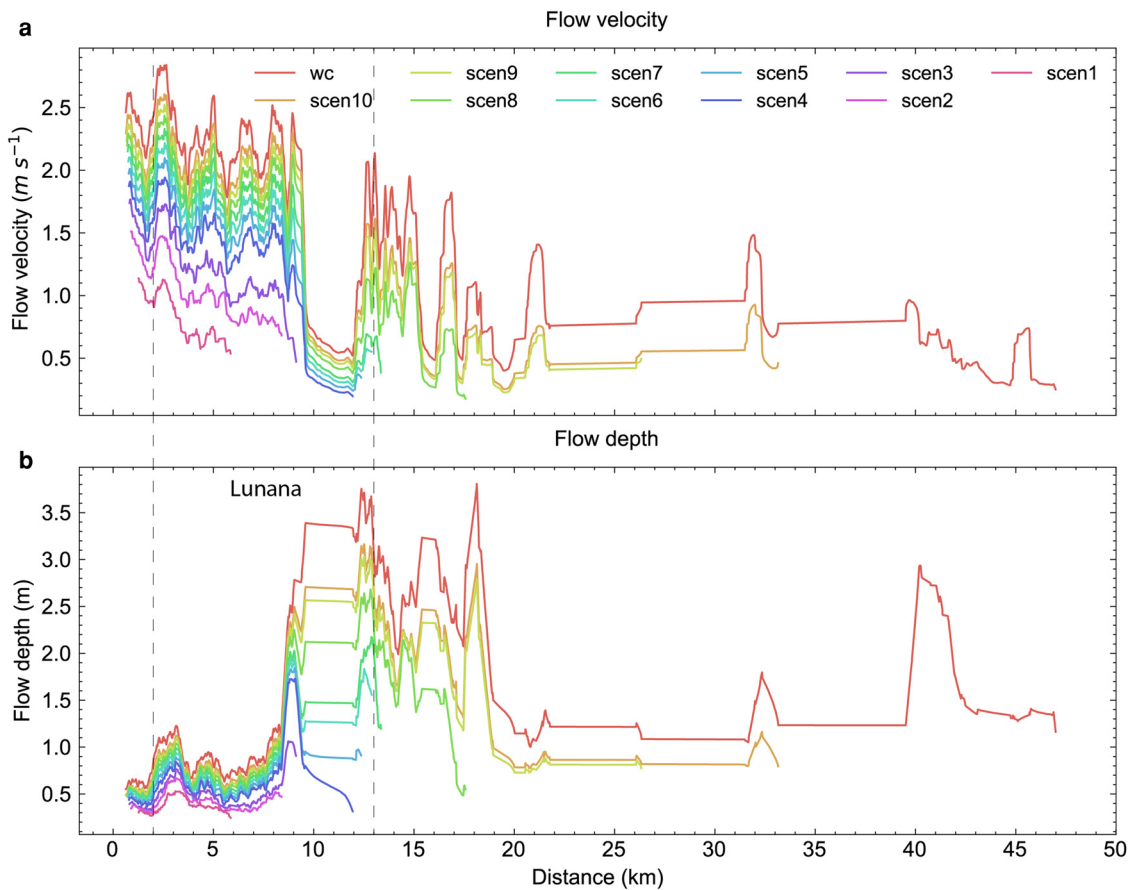


Figure 7. Flow depth and velocity profile every 200 m along the horizontal river centreline under the various scenarios of supraglacial pond outburst floods from Tshojo Glacier. Scenarios are based on pond area, in increments from 10 000–100 000 m² (sc1–sc10) and the worst-case (wc) scenario, which is derived from the maximum total ponded area recorded during the study period. The vertical grey dashed lines show the start and end of the Lunana, i.e. the downstream community inundated under some of the model scenarios.

longitudinal surface gradient of $>2^\circ$, and these areas tend to be associated with the larger ponds (Fig. 5b), supporting past inferences that localised areas of lower longitudinal surface gradient provide preferential conditions for pond formation and growth.

Ice velocities also influence pond distribution, via their impact on the likelihood of drainage (Miles and others, 2020): faster ice flow encourages crevasses to open and ponds to drain, whereas slower flow causes compression, leading to closure of fractures

and thus enables pond persistence and growth (Salerno and others, 2012; Miles and others, 2016, 2017b). Ice velocities on Tshojo Glacier (Figs 5, c) were higher than those observed on the majority of Everest glaciers (Quincey and others, 2007) and elsewhere in Bhutan (Taylor and others, 2022), and Tshojo Glacier's large ponds drained regularly during the study period (Fig. 4). At the same time, the majority of the large, recurrent ponds occur in areas with relatively low surface velocities

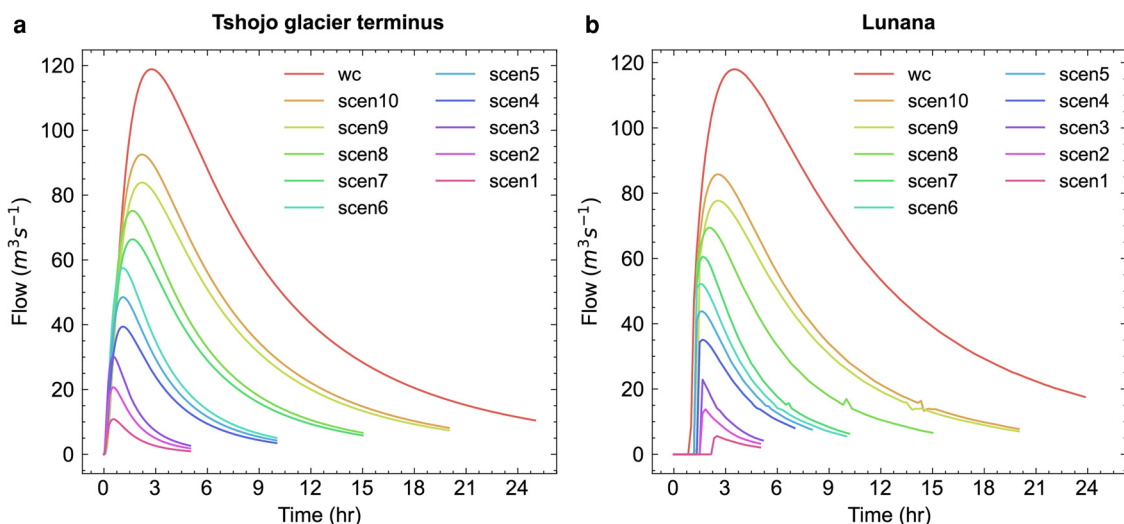


Figure 8. (a) Hydrographs used as the upstream boundary condition, located at the terminus of Tshojo Glacier, and (b) flow hydrograph at Lunana resulted from our multiple scenario pond outburst flood modelling. The locations of Tshojo Glacier and Lunana are shown in Figure 9.

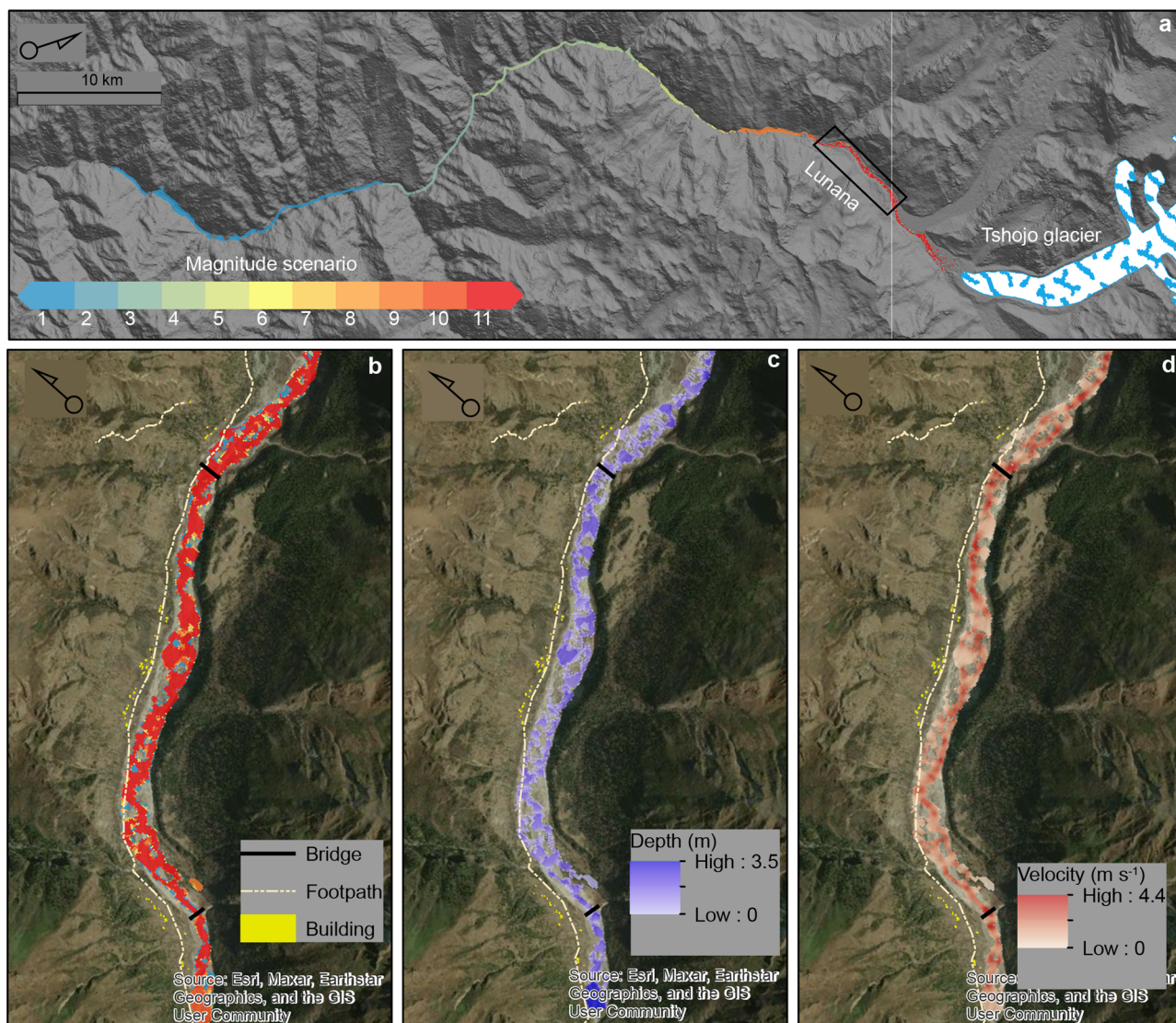


Figure 9. Flood inundation maps for different scenarios of supraglacial pond outburst floods from Tshojo Glacier, detailed in Table 1. (a) Overview of inundation over the entire model domain for each scenario, where a value of 11 means the area is flooded in all scenarios and 1 means the area is only flooded in one scenario. Inundation maps as per (a), focused on: (b) the Lunana region (5–10 km downstream of Tshojo Glacier). (c–d) Flow depth and velocity under the worst-case scenario at the specific locations in Lunana.

(<20 m a⁻¹), meaning that ice inflow and down-glacier pond advection are likely to be limited, and hence ponds occur at comparable locations over time (Fig. 4, Fig. S6). Thus, we suggest that ice velocities on Tshojo Glacier (Fig. 5a) were slow enough to enable large, perched ponds to form, grow and persist in similar locations with minimal down-glacier advection, but were sufficiently fast to regularly open fractures and enable perched ponds to connect to englacial drainage networks (Benn and others, 2001; Liu and others, 2015; Watson and others, 2016, 2017; Miles and others, 2017a). This periodic drainage of Tshojo Glacier's ponds may put a limit on pond growth and coalescence (Benn and others, 2001; Thompson and others, 2012), resulting instead in numerous large, individual, ponds (Fig. 4). Thus, the life cycle of Tshojo Glacier's large ponds is likely influenced by the configuration of the englacial hydrological system and the frequency with which drainage conduits are connected/blocked (Benn and others, 2017). Observations from across the Himalaya document similarly rapid (days to weeks) pond drainage events to those seen on Tshojo Glacier, but pond refilling and drainage recurrence is generally slower, occurring over multiple years, compared to approximately annually at Tshojo Glacier (Benn and others, 2001; Wessels and others,

2002; Watson and others, 2016; Miles and others, 2017a). We suggest that the more regular connection of perched ponds to Tshojo Glacier's englacial hydrology may result from its faster flow, which would produce more fractures and may encourage more rapid evolution, but mapping of its hydrological system would be required to confirm this.

Overall, our data suggest that Tshojo Glacier's ice velocity and longitudinal surface gradient patterns (Fig. 5) enabled large perched ponds to expand over time in the same locations (Fig. 4), with relatively limited down-glacier advection, and regularly connect with the englacial system (Fig. 4), meaning that their drainage and refilling patterns dominated the total ponded area and percentage area coverage on Tshojo Glacier from 2007 onwards (Fig. 2). This is supported by spatial patterns of ponding on the glacier: most of the large ponds occurred between ~3.5 and 8.5 km from the terminus and the small ponds between ~3 and 10 km, which we attribute to the generally higher longitudinal surface gradients closer to the terminus and higher ice velocities up glacier of 10 km (Figs 5a, b). Furthermore, the limit on expansion resulting from the drainage events meant that the ponds did not coalesce to form proglacial lakes, as seen in the Everest region (Watson and others, 2016, 2017) and elsewhere in Bhutan

(Komori, 2008). Thus, Tshojo Glacier has remained at Stage 1 of the Komori (2008) classification, i.e. the appearance and growth of supraglacial lakes on the lower ablation area, for at least 53 years (Fig. S6). This is much longer than its neighbouring glaciers, both in the Lunana area and in the Bhutan-China boarder area more generally, despite the first supraglacial lakes emerging at a similar time across the region (Komori, 2008). Given their proximity and similar aspects, we suggest that differences in climate are unlikely to be sufficient to produce these divergent lake growth trajectories. Instead, we speculate that this may result from Tshojo Glacier's considerably larger total area and high-elevation accumulation area, with multiple tributaries delivering ice to the glacier tongue (Fig. 1), which could offset thinning and pond growth.

4.3. Relationship between ice thickness change and supraglacial ponds

We observed a marked increase in thinning rates between 1975–2000 and 2000–2016 (Figs 6a, b) and the areas of most rapid thinning between 2000 and 2016 coincided with Tshojo Glacier's largest ponds, i.e. between ~3.5 and 8 km up glacier of the terminus (Figs 6b, c). Thus, we suggest that Tshojo Glacier's large ponds contributed to glacier thinning and ice loss, as observed elsewhere in the Himalaya (Liu and others, 2015; Pellicciotti and others, 2015; Watson and others, 2016, 2017; Salerno and others, 2017; Miles and others, 2017a). Furthermore, Tshojo Glacier shows a marked reduction in ice velocities with distance down-glacier (Fig. 5) and maximum thinning rates between ~3.5 and 8 km up glacier from the terminus (Fig. 6), which is indicative of an inverted mass balance gradient (Benn and Lehmkuhl, 2000; Bisset and others, 2020). Inverted mass balance gradients can form on debris-covered glaciers because debris cover is generally thickest nearer the terminus, which suppresses melt, and thins with distance up glacier, which enhances melt at the mid-elevations and leads to a flattening of the surface elevation profile (Quincey and others, 2009; Jouvett and others, 2011; Rowan and others, 2015). However, we also note that Tshojo Glacier has a relatively uniform surface profile with distance up glacier (Fig. 5d) (which has remained similar between 2017 and 2022), whereas as many debris-covered glacier tongues experiencing inverted mass balance gradients have a flat longitudinal surface gradient in their mid-elevations, which becomes increasingly flat over time (Quincey and others, 2007). Furthermore, the area of Tshojo Glacier's tongue in which the ponds are situated has not visibly expanded in the +30 years of Landsat coverage (Fig. S5). Thus, we suggest that Tshojo Glacier has an inverted pattern of thinning with respect to altitude (i.e. peak thinning occurs at mid-elevations), but we did not observe a concomitant upstream expansion of the zone of supraglacial ponding.

4.4. Dominance of larger ponds after 2007

After 2007, there was a marked increase in the area of the largest ponds (Fig. 4): ponds over 30 000 m² were only observed from 2007 onwards and the number of ponds between 20 000 and 30 000 m² quadrupled, compared to 1987–2003 (Fig. 4). The number of ponds of between 1000 and 10 000 m² also increased from 284 (1987–2003) to 343 (2007–2018; Fig. 4), although we did see reduction in pond number from 2017–2020 (Fig. 3b). We suggest a number of potential explanations for this switch to the dominance of larger pond areas after 2007:

- (i) **Differences in satellite imagery:** The change in largest pond area coincides with changing from using Landsat 4–5 TM imagery up to 2003 and Landsat 7 and 8 imagery thereafter

(Table S1). We suggest that this is an unlikely cause, as we visually inspected each NDWI classification output and both the spatial resolution and band wavelengths for Landsat 4–5 and Landsat 7 are identical for bands utilised in the NDWI classification (Table S1). We thus discount this explanation.

- (ii) **Changes in longitudinal gradient:** Surface slope is a key control on pond distribution and characteristics (e.g. Reynolds, 2000; Quincey and others, 2007; Watson and others, 2016), meaning that surface thinning observed on Tshojo Glacier (Fig. 6) could have reduced longitudinal gradients and promoted ponding. However, comparison of longitudinal profiles from Pléiades DSM suggest this is unlikely to be a factor, as the overall surface slope changed little between 2017 and 2022 and does not have a flat profile in the mid elevations.
- (iii) **Changes in ice velocity:** We observed a slow-down in ice velocities between 1988 and 2003, with a subsequent slight speed up, particularly between ~4 and 10 km from the glacier terminus (Fig. 5c). This earlier slowdown may have encouraged pond expansion, by promoting compressional flow, closing fractures, and thus reducing the frequency of drainage events (Salerno and others, 2012; Miles and others, 2016; 2017b). These larger depressions may then have been retained for the rest of the study period, providing the accommodation space for large ponds to form, even once drainage events began occurring regularly (Fig. 4).
- (iv) **Increased air temperature and melt rates:** meteorological conditions are likely to be an important control on pond characteristics at interannual and seasonal timescales (e.g. Miles and others, 2016; Narama and others, 2017; Watson and others, 2017; Miles and others, 2017b, 2017a; Taylor and others, 2022), but the closest meteorological station with data extending back to 2003 is Gyetsa, which is located 80 km from Tshojo Glacier and is therefore not utilised, as it is unlikely to be representative.

Based on the available evidence, we suggest that the emergence of much larger ponds on Tshojo Glacier after 2003 was at least partly facilitated by a slowdown in ice velocities over the preceding years causing conduits to close, reducing the number of drainage events and facilitating pond growth. Once these hollows were formed, then were then reoccupied in subsequent years, and could then be enlarged by feedbacks between pond presence, glacier ablation and pond drainage. However, we underscore the need for meteorological observations proximal to Tshojo Glacier, to comprehensively assess controls on its subglacial pond characteristics, their potential future evolution under a warming climate, and the implications for future GLOF risk.

4.5. Pond outburst flood impacts

In HMA, ~11% of the cumulative historical instances of GLOFs are from supraglacial lakes and almost all GLOF casualties are due to floods from moraine-dammed lakes and supraglacial ponds (Shrestha and others, 2023), making it vital to quantify the potential impact of supraglacial pond outbursts. This is particularly important for Tshojo Glacier, as a recent outburst event, on 29 April 2009, necessitated the evacuation of residents within the Punakha region, although no damage was recorded (Komori and others, 2012). Our modelling scenarios suggest that, aside from the worst-case scenario, floods generated by supraglacial ponds on Tshojo Glacier are small in magnitude (11–93 m³ s⁻¹) and floodwater typically remains within the existing flood plains, resulting to minimal inundation of structures and agricultural land (Fig. 9, Table 1). While this result is

consistent with the minimal damage caused by previous supraglacial pond outburst floods in nearby areas, such as from Halji glacier in north western Nepal (Kropáček and others, 2015), it is important to note that some of the most damaging floods in HMA are small in magnitude. For example, a small, inconspicuous moraine-dammed lake failure event in the transboundary Shakhimardan catchment of Kyrgyzstan and Uzbekistan in the Central Asia had an initial discharge of only $2\text{--}3\text{ m}^3\text{ s}^{-1}$ but increased to $150\text{--}200\text{ m}^3\text{ s}^{-1}$ as it propagated downstream into the valley, resulting in deaths of more than 100 people, while 500–600 went missing and $\sim 14\,000$ people were evacuated (Petraikov and others, 2020). Similarly, the rapid coalescence and subsequent drainage of a series of ponds through the Changri Shar and Khumbu glaciers caused substantial downstream geomorphic change and destroyed major walking routes (Miles and others, 2018). These seemingly low magnitude GLOF possess remarkable mobility and are able to carry a substantial amount of debris (Cook and others, 2018), and, on occasion, can combine with other flood events, such as cloud bursts (Allen and others, 2015). Thus, it is important to recognise the potential for damage resulting from outbursts from Tshojo Glacier's ponds, particularly if similar cascading events occur. This is particularly important given the large proglacial lakes that currently sit upstream of Tshojo Glacier in the Lunana area (Fig. 1) and their potential to generate substantial flood volumes. Furthermore, despite their comparatively small magnitude, our data show that these pond drainage events occur almost annually, meaning they have the potential to impact downstream communities far more regularly than more irregular outbursts from Lunana's large proglacial lakes. Finally, all scenarios impacted footpaths and bridges in the Lunana area, with the worst-case scenario effecting 1.2 km of footpath and 2 bridges (Table 1). Although this damage is minor in the broader context it could have major impacts on local communities: the Lunana area is the remotest part of Bhutan, and so loss of these routes could lead to further isolation from the nearest road access and create challenges in delivering essential aid and responding to a potential flood event.

4.6. GLOF modelling assumptions, sensitivity and recommendations

The shape of the input hydrograph is an essential initial condition in our pond outburst modelling and can significantly affect the resulting flood characteristics and impacts. Despite 11% of reported GLOF events originating from supraglacial ponds (Shrestha and others, 2023), there is a paucity of recorded flood characteristics and empirical relationships to construct hydrographs from such outbursts. Consequently, we used a log-normal distribution curve to construct the hydrograph, assuming a positively skewed flow rate that gradually decreases after peaking. While this assumption is associated with notable uncertainties, we considered multiple (10) outburst flood modelling scenarios from Tshojo Glacier to account for the uncertainty associated with hydrograph. The relatively small predicted magnitudes of the pond outburst events can be at least partly attributed to our assumption of a tunnelled-like drainage system, based on lack of available data to the contrary. However, peak discharge and resulting flood magnitude could greatly surpass the flow we have calculated here if the glacial conduit became obstructed and then rapidly released large amounts of water (Rounce and others, 2017; Miles and others, 2018). Furthermore, we cannot discount the worst-case scenario for flooding from Tshojo Glacier, i.e. that all ponds drain at once, due to a rare, but catastrophic, event such as a large mass movement and/or blockage of a glacier conduit and sudden water release. A recent example

of such an event is the Chamoli rock-ice-avalanche on 7 February 2021 in Uttarakhand, India, which had a magnitude $\sim 27 \times 10^6\text{ m}^3$ (Shugar and others, 2021). We include this extreme, but unlikely scenario, as catastrophic events are difficult to predict but the frequency of these extreme events is expected to increase in the future, due to climate warming and the resultant deglaciation and destabilization of surrounding slopes.

Our area-volume scaling is based on data that includes comparatively few supraglacial ponds (Cook and Quincey, 2015; Watson and others, 2017) and the equation used to estimate peak discharge (Clague and Mathews, 2017) is predominantly focused on large, ice dammed lakes. As such, we highlight the need to collect data on area-volume relationship for supraglacial ponds, both to refine our results at Tshojo Glacier and to enable more accurate modelling of supraglacial pond outburst more broadly. We could not incorporate baseflow in our pond outburst modelling scenarios due to the absence of gauged data within our modelling domain. However, base flow plays a critical role in flood propagation, contributing significantly to channel conveyance and overall flow behaviour such as peak flow, flood duration, and floodplain inundation (Sharma and Mujumdar, 2024). Thus, we recommend installation of water level sensors to capture base flow variations, to inform GLOF modelling both at Tshojo Glacier and the lakes upstream at Lunana. Future GLOF modelling work at Tshojo Glacier should also be conducted in conjunction scenarios for Lunana's largest lakes, to identify the possibility for cascading GLOF events and their potential impacts.

The flood volume resulting from Tshojo Glacier's supraglacial pond outburst flood on 29 April 2009 was estimated to be $\sim 0.5 \times 10^6\text{ m}^3$, which is approximately equivalent to our Scenario 5 (Table 2). However, the 2009 estimation was made ~ 70 km downstream, in Punakha, (Komori and others, 2012), so the actual flood volume and discharge from the event at Tshojo Glacier itself is unknown. Available data suggest that the pond drained rapidly: it was present in satellite imagery from 24 April 2009 image, fully drained by the next available image from 19 May 2009, and had started to refill in December 2009 (Yamanokuchi and others, 2011). This supports our modelling approach of sudden drainage of individual ponds, informed by the range of pond sizes we observed on Tshojo Glacier during the study period. Future work should use high temporal resolution satellite imagery (e.g. PlanetScope) to further constrain pond drainage timeframes, and hence refine our modelled outburst hydrographs. Furthermore, we lack comprehensive data on vital model input parameters, such as flow rate, depth, and velocity, even though the 2009 event is considered a contemporary example of a GLOF in Bhutan. This data deficiency makes it challenging to calibrate our modelled outburst floods and so our scenario-based approach should be considered as a guide to potential inundation extent and location, based on the data that are currently available.

In this study, we assume clear water flow in HEC-RAS 2-D model, as our aim is to provide a first-pass assessment of potential pond outburst flood volumes and extents and HEC-RAS provides a computationally affordable tool to conduct this assessment, which has been used in many comparable studies (e.g. Klimeš and others, 2014; Maskey and others, 2020). However, outburst floods may contain significant amount of debris (Miles and others, 2018), which may mean that our clear water results underestimate both flow volume and flow rate, and hence inundation extent. Models like r.avaflo (Mergili and others, 2017) and RAMMS (Christen and others, 2010) have the capability to model bed erosion and the resulting debris/mud flow, but we lack the necessary input information for Tshojo Glacier. Thus, future work could evaluate the impact of clear vs debris-laden flow, in combination with field data to inform parameter choices.

Due to the absence of open access, high-resolution DEMs that adequately cover the Lunana region, our outburst simulations are based on medium resolution ALOS-PALSAR DEM data. Our sensitivity analysis for part of our model domain suggest that key modelled GLOF output parameters (total and peak flow, and inundation extent) showed limited variation between the ALOS-PALSAR DEM (30 m resolution) and the high-resolution HMA 8 m DEM (Fig. S8). However, our comparison is confined to the Lunana region, which is a relatively flat part of our model domain and so discrepancies could be higher further downstream, where the topography is steeper (Wang and others, 2016; Liu and others, 2019; Rinzin and others, 2023). Furthermore, the detailed pattern of inundation and parameters such as flood depth does vary between the different DEMs. Thus, our modelling results provide an overview of potential flood routing from Tshojo Glacier, using the datasets currently available, but could be further improved and refined by acquiring and incorporating high-resolution DEMs, e.g. from site-specific UAV surveys. Our sensitivity analysis shows that flow arrival time is highly sensitive to the Manning's n value and that this impact increases with distance downstream (Fig. S7), which has important implications for developing and locating early warning systems (Carey and others, 2011). Thus, we caution against only using coarse-scale (i.e. global to regional scale) land-use products to derive Manning's n values and instead recommend generating basin-specific data from high-resolution satellite imagery sources such as PlanetScope.

Despite the limitations noted above, our inundation map, based on first-order hydraulic modelling, provides a basis for further modelling of outburst scenarios from Tshojo Glacier's supraglacial ponds. Future modelling work should be informed by monitoring of changes in ponded area and, in particular the size of Tshojo Glacier's largest ponds, as climate warms and the glacier evolves. This is particularly important given the frequent drainage of Tshojo Glacier's largest ponds (Figs 4, 5), their impact on total ponded area (Fig. 2), their persistence (Fig. S6), and their potential impacts on downstream populations and HEP stations (Fig. 9 and Table 1). Overall, our work underscores the threat posed by GLOFs to communities in the Lunana region (Rinzin and others, 2023) and Bhutan more broadly (Taylor and others, 2023) and highlights the urgent need to quantify their evolving threat in a warming world.

5. Conclusions

Overall, our data show that ponded area and its variability increased substantially between 1987 and 2020 on Tshojo Glacier, with a marked shift occurring between 2003 and 2007. These temporal patterns were predominantly driven by the area of the largest ponds: from 2007 onwards, we observed much larger ponds, which drained regularly. Declassified satellite imagery indicates that these large ponds have occupied the same locations since at least 1967 and that Tshojo Glacier has remained in the first stage of proglacial lake development (i.e. isolated ponds on its surface) during this time, in contrast to the neighbouring glaciers in the Lunana region. We attribute the limited pond coalescence on Tshojo Glacier to its moderate longitudinal surface gradient and ice velocities: these factors are low enough to promote the formation of large ponds, but are insufficient for ponds to coalesce, while velocities are high enough to facilitate regular drainage events, thus limiting pond growth. We suggest that the step-change in the area of Tshojo Glacier's largest ponds between 2003 and 2007 may have been linked to reduced ice velocities during the 1990s, which reduced drainage events and thus promoted growth. However, changes in climate are a potentially important driving factor that could not be investigated, as the closest available meteorological station with data pre-2003 was located ~80 km from Tshojo Glacier. Numerical

modelling shows that the flood wave from our pond outburst scenarios could reach between ~6 km (scenario1) and 47 km (worst-case scenario) downstream of Tshojo Glacier's terminus. In all cases, the flood waves reached the settlement of Lunana within an hour of initiation and damage occurred to bridges, agricultural land and footpaths. Although these impacts may appear minor, they could isolate already very remote communities and prevent the delivery of emergency aid. Furthermore, pond outbursts from Tshojo could potentially be magnified by combining with other flood events, such as cloud bursts or drainage of Lunana's large glacier lakes upstream. Our work highlights a number of key areas where we could improve GLOF simulations, both at Tshojo Glacier and from supraglacial outburst floods in general, including: incorporating base flow data; improved knowledge of water routing from burst ponds; specific volume-area scaling relationships for supraglacial ponds; evaluation of the impact of clear vs debris-laden flow; and high resolution data to determine how rapidly ponds drain. Sensitivity analysis suggested that DEM resolution did not markedly impact our results in the Lunana area, but could not be evaluated across the entire domain due to data gaps, and that the Manning's n value is an important control on arrival time and hence for the development of early warning systems. Overall, our results highlight the need to continue monitoring the evolution of Tshojo Glacier and its large ponds, to better understand GLOF threat in Bhutan and how it will evolve as climate warms.

Data availability. Data on ice velocities, the longitudinal gradient of the glacier surface and glacier thickness change are freely available online and the sources are specified in the methods section. Furthermore information on ITS LIVE data processing and resultant dataset are available in Gardner and others, 2018 and via this web link: http://its-live-data.jpl.nasa.gov/s3.amazonaws.com/documentation/ITS_LIVE-Regional-Glacier-and-Ice-Sheet-Surface-Velocities.pdf. Further details on the glacier thickness change dataset are available at: https://nsidc.org/sites/default/files/hma_glacier_dh_mosaics-v001-userguide_1.pdf. Landsat images are freely available online via the USGS Earth Explorer. Shapefiles of supraglacial pond area are available on request from the corresponding author (Rachel.carr@newcastle.ac.uk).

Supplementary material. The supplementary material for this article can be found at <https://doi.org/10.1017/jog.2024.62>.

References

- Allen SK, Rastner P, Arora M, Huggel C and Stoffel M (2015) Lake outburst and debris flow disaster at Kedarnath, June 2013: hydrometeorological triggering and topographic predisposition. *Landslides* 13(6), 1479–1491. doi: [10.1007/s10346-015-0584-3](https://doi.org/10.1007/s10346-015-0584-3)
- Arcement GJ and Schneider VR (1989) *Guide for Selecting Manning's Roughness Coefficients for Natural Channels and Flood Plains*. Washington, DC: US Government Printing Office.
- Benn D and 9 others (2012) Response of debris-covered glaciers in the Mount Everest region to recent warming, and implications for outburst flood hazards. *Earth-Science Reviews* 114(1), 156–174. doi: [10.1016/j.earscirev.2012.03.008](https://doi.org/10.1016/j.earscirev.2012.03.008)
- Benn DI and 5 others (2017) Structure and evolution of the drainage system of a Himalayan debris-covered glacier, and its relationship with patterns of mass loss. *The Cryosphere* 11(5), 2247–2264. doi: [10.5194/tc-11-2247-2017](https://doi.org/10.5194/tc-11-2247-2017)
- Benn DI and Lehmkuhl F (2000) Mass balance and equilibrium-line altitudes of glaciers in high-mountain environments. *Quaternary International* 65, 15–29. doi: [10.1016/S1040-6182\(99\)00034-8](https://doi.org/10.1016/S1040-6182(99)00034-8)
- Benn DI, Wiseman S and Hands KA (2001) Growth and drainage of supraglacial lakes on debris-mantled Ngozumpa Glacier, Khumbu Himal, Nepal. *Journal of Glaciology* 47(159), 626–638. doi: [10.3189/172756501781831729](https://doi.org/10.3189/172756501781831729)
- Berthier E and 8 others (2024) The Pléiades Glacier observatory: high resolution digital elevation models and ortho-imagery to monitor glacier change. *EGU sphere* 2024, 1–25. doi: [10.5194/egusphere-2024-250](https://doi.org/10.5194/egusphere-2024-250)
- Beyer RA, Alexandrov O and McMichael S (2018) The Ames Stereo Pipeline: NASA's open source software for deriving and processing terrain data. *Earth and Space Science* 5(9), 537–548. doi: [10.1029/2018EA000409](https://doi.org/10.1029/2018EA000409)

- Bisset RR** and 5 others (2020) Reversed surface-mass-balance gradients on Himalayan debris-covered glaciers inferred from remote sensing. *Remote Sensing* **12**(10), 1563. doi: [10.3390/rs12101563](https://doi.org/10.3390/rs12101563)
- Bolch T** and 5 others (2011) Identification of potentially dangerous glacial lakes in the northern Tien Shan. *Natural Hazards* **59**(3), 1691–1714. doi: [10.1007/s11069-011-9860-2](https://doi.org/10.1007/s11069-011-9860-2)
- Bolch T** and 10 others (2012) The state and fate of Himalayan glaciers. *Science (New York, N.Y.)* **336**(6079), 310–314. doi: [10.1126/science.1215828](https://doi.org/10.1126/science.1215828)
- Brown CF** and 10 others (2022) Dynamic world, near real-time global 10 m land use land cover mapping. *Scientific Data* **9**(1), 251. doi: [10.1038/s41597-022-01307-4](https://doi.org/10.1038/s41597-022-01307-4)
- Brun F, Berthier E, Wagnon P, Kääb A and Treichler D** (2017) A spatially resolved estimate of High Mountain Asia glacier mass balances from 2000 to 2016. *Nature Geoscience* **10**(9), 668–673. doi: [10.1038/NGEO2999](https://doi.org/10.1038/NGEO2999)
- Carey M, Huggel C, Bury J, Portocarrero C and Haerberli W** (2011) An integrated socio-environmental framework for glacier hazard management and climate change adaptation: lessons from Lake 513, Cordillera Blanca, Peru. *Climatic Change* **112**(3–4), 733–767. doi: [10.1007/s10584-011-0249-8](https://doi.org/10.1007/s10584-011-0249-8)
- Carrivick JL and Tweed FS** (2013) Proglacial lakes: character, behaviour and geological importance. *Quaternary Science Reviews* **78**, 34–52. doi: [10.1016/j.quascirev.2013.07.028](https://doi.org/10.1016/j.quascirev.2013.07.028)
- Carrivick JL and Tweed FS** (2016) A global assessment of the societal impacts of glacier outburst floods. *Global and Planetary Change* **144**, 1–16. doi: [10.1016/j.gloplacha.2016.07.001](https://doi.org/10.1016/j.gloplacha.2016.07.001)
- CEIWR-HEC** (2021) *HEC-RAS River Analysis System. 2D Modeling User's Manual*. Davis, USA: Institute for Water Resources, Hydrologic Engineering Center.
- Chand MB and Watanabe T** (2019) Development of supraglacial ponds in the Everest Region, Nepal, between 1989 and 2018. *Remote Sensing* **11**(9), 1058. doi: [10.3390/rs11091058](https://doi.org/10.3390/rs11091058)
- Christen M, Kowalski J and Bartelt P** (2010) RAMMS: numerical simulation of dense snow avalanches in three-dimensional terrain. *Cold Regions Science and Technology* **63**(1–2), 1–14. doi: [10.1016/j.coldregions.2010.04.005](https://doi.org/10.1016/j.coldregions.2010.04.005)
- Clague JJ and Mathews WH** (2017) The magnitude of Jökulhlaups. *Journal of Glaciology* **12**(66), 501–504. doi: [10.3189/s0022143000031907](https://doi.org/10.3189/s0022143000031907)
- Cook S and Quincey D** (2015) Estimating the volume of Alpine glacial lakes. *Earth Surface Dynamics* **3**, 909–940. doi: [10.5194/esurf-d-3-909-2015](https://doi.org/10.5194/esurf-d-3-909-2015)
- Cook KL, Andermann C, Gimbert F, Adhikari BR and Hovius N** (2018) Glacial lake outburst floods as drivers of fluvial erosion in the Himalaya. *Science (New York, N.Y.)* **362**(6410), 53–57. doi: [10.1126/science.aat4981](https://doi.org/10.1126/science.aat4981)
- Dorji U, Olesen JE, Böcher PK and Seidenkrantz MS** (2016) Spatial variation of temperature and precipitation in Bhutan and links to vegetation and land cover. *Mountain Research and Development* **36**(1), 66–79. doi: [10.1659/mrd-journal-d-15-00020.1](https://doi.org/10.1659/mrd-journal-d-15-00020.1)
- Emmer A** and 10 others (2022) Progress and challenges in glacial lake outburst flood research (2017–2021): a research community perspective. *Natural Hazards and Earth System Sciences* **22**(9), 3041–3061. doi: [10.5194/nhess-22-3041-2022](https://doi.org/10.5194/nhess-22-3041-2022)
- Fujita K, Suzuki R, Nuimura T and Sakai A** (2008) Performance of ASTER and SRTM DEMs, and their potential for assessing glacial lakes in the Lunana region, Bhutan Himalaya. *Journal of Glaciology* **54**(185), 220–228. doi: [10.3189/002214308784886162](https://doi.org/10.3189/002214308784886162)
- Fujita K** and 6 others (2013) Potential flood volume of Himalayan glacial lakes. *Natural Hazards & Earth System Sciences* **13**(7), 1827–1839. doi: [10.5194/nhess-13-1827-2013](https://doi.org/10.5194/nhess-13-1827-2013)
- Gardelle J, Arnaud Y and Berthier E** (2011) Contrasted evolution of glacial lakes along the Hindu Kush Himalaya mountain range between 1990 and 2009. *Global and Planetary Change* **75**(1–2), 47–55. doi: [10.1016/j.gloplacha.2010.10.003](https://doi.org/10.1016/j.gloplacha.2010.10.003)
- Gardner AS** and 6 others (2018) Increased West Antarctic and unchanged East Antarctic ice discharge over the last 7 years. *The Cryosphere* **12**(2), 521–547. doi: [10.5194/tc-12-521-2018](https://doi.org/10.5194/tc-12-521-2018)
- Hirschmuller H** (2007) Stereo processing by semiglobal matching and mutual information. *IEEE Transactions on Pattern Analysis and Machine Intelligence* **30**(2), 328–341. doi: [10.1109/TPAMI.2007.1166](https://doi.org/10.1109/TPAMI.2007.1166)
- Huggel C** and 7 others (2020) An integrative and joint approach to climate impacts, hydrological risks and adaptation in the Indian Himalayan region. In Dimri AP, Bookhagen B, Stoffel M and Yasunari Y (eds), *Himalayan Weather and Climate and Their Impact on the Environment*. Switzerland: Springer Cham, pp. 553–573. doi: [10.1007/978-3-030-29684-1_26](https://doi.org/10.1007/978-3-030-29684-1_26)
- Hugonnet R** and 10 others (2021) Accelerated global glacier mass loss in the early twenty-first century. *Nature* **592**(7856), 726–731. doi: [10.1038/s41586-021-03436-z](https://doi.org/10.1038/s41586-021-03436-z)
- Immerzeel WW** and 10 others (2020) Importance and vulnerability of the world's water towers. *Nature* **577**(7790), 364–369. doi: [10.1038/s41586-019-1822-y](https://doi.org/10.1038/s41586-019-1822-y)
- Immerzeel WW, van Beek LPH and Bierkens MFP** (2010) Climate change will affect the Asian water towers. *Science (New York, N.Y.)* **328**(5984), 1382. doi: [10.1126/science.1183188](https://doi.org/10.1126/science.1183188)
- Jha LK and Khare D** (2017) Detection and delineation of glacial lakes and identification of potentially dangerous lakes of Dhauliganga basin in the Himalaya by remote sensing techniques. *Natural Hazards* **85**(1), 301–327. doi: [10.1007/s11069-016-2565-9](https://doi.org/10.1007/s11069-016-2565-9)
- Jouvet G, Huss M, Funk M and Blatter H** (2011) Modelling the retreat of Grosser Aletschgletscher, Switzerland, in a changing climate. *Journal of Glaciology* **57**(206), 1033–1045. doi: [10.3189/002214311798843359](https://doi.org/10.3189/002214311798843359)
- Khadka N, Zhang G and Thakuri S** (2018) Glacial lakes in the Nepal Himalaya: inventory and decadal dynamics (1977–2017). *Remote Sensing* **10**(12), 1913. doi: [10.3390/rs10121913](https://doi.org/10.3390/rs10121913)
- Klímeš J, Benešová M, Vilímek V, Bouška P and Cochachin Rapre A** (2014) The reconstruction of a glacial lake outburst flood using HEC-RAS and its significance for future hazard assessments: an example from Lake 513 in the Cordillera Blanca, Peru. *Natural Hazards* **71**, 1617–1638. doi: [10.1007/s11069-013-0968-4](https://doi.org/10.1007/s11069-013-0968-4)
- Kneib M** and 6 others (2021) Interannual dynamics of ice cliff populations on debris-covered glaciers from remote sensing observations and stochastic modeling. *Journal of Geophysical Research: Earth Surface* **126**(10), e2021JF006179. doi: [10.1029/2021JF006179](https://doi.org/10.1029/2021JF006179)
- Komori J** (2008) Recent expansions of glacial lakes in the Bhutan Himalayas. *Quaternary International* **184**(1), 177–186. doi: [10.1016/j.quaint.2007.09.012](https://doi.org/10.1016/j.quaint.2007.09.012)
- Komori J and Tshering P** (2010) *Pictorial 1: Flood from Tshojo Glacier in the Bhutan Himalaya on April 29, 2009*.
- Komori J, Koike T, Yamanokuchi T and Tshering P** (2012) Glacial lake outburst events in the Bhutan Himalayas. *Global Environment Research* **16**, 59–70. doi: [10.1007/s41748-021-00230-9](https://doi.org/10.1007/s41748-021-00230-9)
- Kropáček J** and 9 others (2015) Repeated glacial lake outburst flood threatening the oldest Buddhist monastery in north-western Nepal. *Natural Hazards and Earth System Sciences* **15**(10), 2425–2437. doi: [10.5194/nhess-15-2425-2015](https://doi.org/10.5194/nhess-15-2425-2015)
- Lillesand TM** (2008) *Remote Sensing and Image Interpretation*, 6th edn. Hoboken, N.J.: John Wiley & Sons.
- Liu K** and 5 others (2019) Global open-access DEM performances in Earth's most rugged region high mountain Asia: a multi-level assessment. *Geomorphology* **338**, 16–26. doi: [10.1016/j.geomorph.2019.04.012](https://doi.org/10.1016/j.geomorph.2019.04.012)
- Liu Q, Mayer C and Liu S** (2015) Distribution and interannual variability of supraglacial lakes on debris-covered glaciers in the Khan Tengri-Tumor Mountains, Central Asia. *Environmental Research Letters* **10**(1), 014014. doi: [10.1088/1748-9326/10/1/014014](https://doi.org/10.1088/1748-9326/10/1/014014)
- Maskey S, Kayastha RB and Kayastha R** (2020) Glacial lakes outburst floods (GLOFs) modelling of Thulagi and lower Barun glacial lakes of Nepalese Himalaya. *Progress in Disaster Science* **7**, 100106. doi: [10.1016/j.pdisas.2020.100106](https://doi.org/10.1016/j.pdisas.2020.100106)
- Maurer J** and 6 others (2020) Seismic observations, numerical modeling, and geomorphic analysis of a glacier lake outburst flood in the Himalayas. *Science Advances* **6**(38), eaba3645. doi: [10.1126/sciadv.aba3645](https://doi.org/10.1126/sciadv.aba3645)
- Maurer J, Rupper S and Schaefer J** (2019a) High Mountain Asia Glacier Thickness Change Mosaics from Multi-Sensor DEMs, Version 1.
- Maurer JM, Schaefer J, Rupper S and Corley A** (2019b) Acceleration of ice loss across the Himalayas over the past 40 years. *Science Advances* **5**(6), eaav7266. doi: [10.1126/sciadv.aav7266](https://doi.org/10.1126/sciadv.aav7266)
- McFeeters SK** (1996) The use of the normalized difference water Index (NDWI) in the delineation of open water features. *International Journal of Remote Sensing* **17**(7), 1425–1432. doi: [10.1080/01431169608948714](https://doi.org/10.1080/01431169608948714)
- Mergili M, Fischer J-T, Krenn J and Pudasaini SP** (2017) Ravaflow v1, an advanced open-source computational framework for the propagation and interaction of two-phase mass flows. *Geoscientific Model Development* **10**(2), 553–569. doi: [10.5194/gmd-10-553-2017](https://doi.org/10.5194/gmd-10-553-2017)
- Miles ES** and 5 others (2016) Refined energy-balance modelling of a supraglacial pond, Langtang Khola, Nepal. *Annals of Glaciology* **57**(71), 29–40. doi: [10.3189/2016AoG17A421](https://doi.org/10.3189/2016AoG17A421)

- Miles E, Willis I, Arnold N, Steiner J and Pellicciotti F (2017a) Spatial, seasonal and interannual variability of supraglacial ponds in the Langtang Valley of Nepal, 1999–2013. *Journal of Glaciology* **63**(237), 88–105. doi: [10.1017/jog.2016.120](https://doi.org/10.1017/jog.2016.120)
- Miles ES and 6 others (2017b) Pond dynamics and supraglacial-englacial connectivity on debris-covered liruung glacier, Nepal. *Frontiers in Earth Science* **5**, 69. doi: [10.3389/feart.2017.00069](https://doi.org/10.3389/feart.2017.00069)
- Miles ES and 8 others (2018) Glacial and geomorphic effects of a supraglacial lake drainage and outburst event, Everest region, Nepal Himalaya. *The Cryosphere* **12**(12), 3891–3905. doi: [10.5194/tc-12-3891-2018](https://doi.org/10.5194/tc-12-3891-2018)
- Miles KE and 5 others (2020) Hydrology of debris-covered glaciers in High Mountain Asia. *Earth-Science Reviews* **207**, 103212. doi: [10.1016/j.ear-scirev.2020.103212](https://doi.org/10.1016/j.ear-scirev.2020.103212)
- Millan R, Mouginot J, Rabatel A and Morlighem M (2022) Ice velocity and thickness of the world's glaciers. *Nature Geoscience* **15**(2), 124–129. doi: [10.1038/s41561-021-00885-z](https://doi.org/10.1038/s41561-021-00885-z)
- Narama C and 6 others (2017) Seasonal drainage of supraglacial lakes on debris-covered glaciers in the Tien Shan Mountains, Central Asia. *Geomorphology* **286**, 133–142. doi: [10.1016/j.geomorph.2017.03.002](https://doi.org/10.1016/j.geomorph.2017.03.002)
- Nie Y and 6 others (2017) A regional-scale assessment of Himalayan glacial lake changes using satellite observations from 1990 to 2015. *Remote Sensing of Environment* **189**, 1–13. doi: [10.1016/j.rse.2016.11.008](https://doi.org/10.1016/j.rse.2016.11.008)
- Nie Y and 10 others (2021) Glacial change and hydrological implications in the Himalaya and Karakoram. *Nature Reviews Earth & Environment*, **2**(2), 91–106. doi: [10.1038/s43017-020-00124-w](https://doi.org/10.1038/s43017-020-00124-w)
- Pellicciotti F and 5 others (2015) Mass-balance changes of the debris-covered glaciers in the Langtang Himal, Nepal, from 1974 to 1999. *Journal of Glaciology* **61**(226), 373–386. doi: [10.3189/2015JogG13J237](https://doi.org/10.3189/2015JogG13J237)
- Petrakov DA and 10 others (2020) Putting the poorly documented 1998 GLOF disaster in Shakhimardan River valley (Alay Range, Kyrgyzstan/Uzbekistan) into perspective. *Science of The Total Environment* **724**, 138287. doi: [10.1016/j.scitotenv.2020.138287](https://doi.org/10.1016/j.scitotenv.2020.138287)
- Pritchard HD (2019) Asia's shrinking glaciers protect large populations from drought stress. *Nature* **569**(7758), 649–654. doi: [10.1038/s41586-019-1240-1](https://doi.org/10.1038/s41586-019-1240-1)
- Quincey D and 6 others (2007) Early recognition of glacial lake hazards in the Himalaya using remote sensing datasets. *Global and Planetary Change* **56**(1), 137–152. doi: [10.1016/j.gloplacha.2006.07.013](https://doi.org/10.1016/j.gloplacha.2006.07.013)
- Quincey D, Luckman A and Benn D (2009) Quantification of Everest region glacier velocities between 1992 and 2002, using satellite radar interferometry and feature tracking. *Journal of Glaciology* **55**(192), 596–606. doi: [10.3189/002214309789470987](https://doi.org/10.3189/002214309789470987)
- Reynolds JM (2000) On the formation of supraglacial lakes on debris-covered glaciers. IAHS Publication 264 'Debris-covered Glaciers: Proceedings of an International Workshop Held at Seattle, Washington, USA'. 153–164.
- RGoB (2011) Bhutan National Human Development Report – Sustaining Progress: Rising to the Climate Challenge. Government Report. Available at http://hdr.undp.org/sites/default/files/bhutan_nhdr_2011.pdf (accessed).
- Richardson SD and Reynolds JM (2000) An overview of glacial hazards in the Himalayas. *Quaternary International* **56**, 31–47. doi: [10.1016/S1040-6182\(99\)00035-X](https://doi.org/10.1016/S1040-6182(99)00035-X)
- Rinzin S and 6 others (2023) GLOF hazard, exposure, vulnerability, and risk assessment of potentially dangerous glacial lakes in the Bhutan Himalaya. *Journal of Hydrology* **619**, 129311. doi: [10.1016/j.jhydrol.2023.129311](https://doi.org/10.1016/j.jhydrol.2023.129311)
- Rounce DR, McKinney DC, Lala JM, Byers AC and Watson CS (2016) A new remote hazard and risk assessment framework for glacial lakes in the Nepal Himalaya. *Hydrology and Earth System Sciences* **20**(9), 3455–3475. doi: [10.5194/hess-20-3455-2016](https://doi.org/10.5194/hess-20-3455-2016)
- Rounce DR, Byers AC, Byers EA and McKinney DC (2017) Brief communication: observations of a glacier outburst flood from Lhotse Glacier, Everest area, Nepal. *The Cryosphere* **11**(1), 443–449. doi: [10.5194/tc-11-443-2017](https://doi.org/10.5194/tc-11-443-2017)
- Rounce DR, Hock R and Shean DE (2020) Glacier mass change in High Mountain Asia through 2100 using the open-source python glacier evolution model (PyGEM). *Frontiers in Earth Science* **7**, 331. doi: [10.3389/feart.2019.00331](https://doi.org/10.3389/feart.2019.00331)
- Rowan AV, Egholm DL, Quincey DJ and Glasser NF (2015) Modelling the feedbacks between mass balance, ice flow and debris transport to predict the response to climate change of debris-covered glaciers in the Himalaya. *Earth and Planetary Science Letters* **430**, 427–438. doi: [10.1016/j.epsl.2015.09.004](https://doi.org/10.1016/j.epsl.2015.09.004)
- Sakai A and Fujita K (2010) Formation conditions of supraglacial lakes on debris-covered glaciers in the Himalaya. *Journal of Glaciology* **56**(195), 177–181. doi: [10.3189/002214310791190785](https://doi.org/10.3189/002214310791190785)
- Sakai A, Takeuchi N, Fujita K and Nakawo M (2000) Role of supraglacial ponds in the ablation process of a debris-covered glacier in the Nepal Himalayas. IAHS Publication 264 'Debris-covered Glaciers: Proceedings of an International Workshop Held at Seattle, Washington, USA', pp. 119–132.
- Sakai A, Nishimura K, Kadota T and Takeuchi N (2009) Onset of calving at supraglacial lakes on debris-covered glaciers of the Nepal Himalaya. *Journal of Glaciology* **55**(193), 909–917. doi: [10.3189/002214309790152555](https://doi.org/10.3189/002214309790152555)
- Salerno F and 6 others (2012) Glacial lake distribution in the Mount Everest region: uncertainty of measurement and conditions of formation. *Global and Planetary Change* **92–93**, 30–39. doi: [10.1016/j.gloplacha.2012.04.001](https://doi.org/10.1016/j.gloplacha.2012.04.001)
- Salerno F and 6 others (2017) Debris-covered glacier anomaly? Morphological factors controlling changes in the mass balance, surface area, terminus position, and snow line altitude of Himalayan glaciers. *Earth and Planetary Science Letters* **471**, 19–31. doi: [10.1016/j.epsl.2017.04.039](https://doi.org/10.1016/j.epsl.2017.04.039)
- Sharma S and Mujumdar PP (2024) Baseflow significantly contributes to river floods in Peninsular India. *Scientific Reports* **14**(1), 1251. doi: [10.1038/s41598-024-51850-w](https://doi.org/10.1038/s41598-024-51850-w)
- Shean D (2017) High Mountain Asia 8-meter DEM Mosaics Derived from Optical Imagery, Version 1 [Data Set].
- Shean DE and 5 others (2020) A systematic, regional assessment of high mountain Asia glacier mass balance. *Frontiers in Earth Science* **7**, 363. doi: [10.3389/feart.2019.00363](https://doi.org/10.3389/feart.2019.00363)
- Shrestha F and 9 others (2023) A comprehensive and version-controlled database of glacial lake outburst floods in High Mountain Asia. *Earth System Science Data* **15**(9), 3941–3961. doi: [10.5194/essd-15-3941-2023](https://doi.org/10.5194/essd-15-3941-2023)
- Shugar DH and 9 others (2020) Rapid worldwide growth of glacial lakes since 1990. *Nature Climate Change* **10**(10), 939–945. doi: [10.1038/s41558-020-0855-4](https://doi.org/10.1038/s41558-020-0855-4)
- Shugar D and 10 others (2021) A massive rock and ice avalanche caused the 2021 disaster at Chamoli, Indian Himalaya. *Science (New York, N.Y.)* **373**(6552), 300–306. doi: [10.1126/science.abb4455](https://doi.org/10.1126/science.abb4455)
- Steiner JF, Buri P, Miles ES, Ragettli S and Pellicciotti F (2019) Supraglacial ice cliffs and ponds on debris-covered glaciers: spatio-temporal distribution and characteristics. *Journal of Glaciology* **65**(252), 617–632. doi: [10.1017/jog.2019.40](https://doi.org/10.1017/jog.2019.40)
- Strickland R, Covington M, Gulley J, Kayastha R and Blackstock J (2023) Englacial drainage drives positive feedback depression growth on the debris-covered Ngozumpa Glacier, Nepal. *Geophysical Research Letters* **50**(16), e2023GL104389. doi: [10.1029/2023GL104389](https://doi.org/10.1029/2023GL104389)
- Taylor CJ, Carr JR and Rounce DR (2022) Short-term spatiotemporal supraglacial pond and ice cliff changes in the Bhutan-Tibet border region from 2016–2018. *Journal of Glaciology* **68**(267), 101–113. doi: [10.1017/jog.2021.76](https://doi.org/10.1017/jog.2021.76)
- Taylor C, Robinson T, Dunning S, Carr J and Westoby M (2023) Glacial lake outburst floods threaten millions globally. *Nature Communications* **14**(1), 487. doi: [10.1038/s41467-023-36033-x](https://doi.org/10.1038/s41467-023-36033-x)
- Thompson SS, Benn DI, Dennis K and Luckman A (2012) A rapidly growing moraine-dammed glacial lake on Ngozumpa Glacier, Nepal. *Geomorphology* **145**, 1–11. doi: [10.1016/j.geomorph.2011.08.015](https://doi.org/10.1016/j.geomorph.2011.08.015)
- Uddin K (2021) Land cover of HKH region. Available at <http://rds.icimod.org/Home/DataDetail?metadataId=1972511>
- UNDPBhutan (2011) Fact Sheet: Outcome 3: Reduced human and material losses in vulnerable communities in the Punakha-Wangdue Valley through GLOF early warnings.
- Wang W, Xiang Y, Gao Y, Lu A and Yao T (2015) Rapid expansion of glacial lakes caused by climate and glacier retreat in the central Himalayas. *Hydrological Processes* **29**(6), 859–874. doi: [10.1002/hyp.10199](https://doi.org/10.1002/hyp.10199)
- Wang X, Liu Q, Liu S, Wei J and Jiang Z (2016) Heterogeneity of glacial lake expansion and its contrasting signals with climate change in Tarim Basin, Central Asia. *Environmental Earth Sciences* **75**(8), 1–11. doi: [10.1007/s12665-016-5498-4](https://doi.org/10.1007/s12665-016-5498-4)
- Watson CS, Quincey DJ, Carrivick JL and Smith MW (2016) The dynamics of supraglacial ponds in the Everest region, central Himalaya. *Global and Planetary Change* **142**(Supplement C), 14–27. doi: [10.1016/j.gloplacha.2016.04.008](https://doi.org/10.1016/j.gloplacha.2016.04.008)
- Watson CS and 5 others (2017) Heterogeneous water storage and thermal regime of supraglacial ponds on debris-covered glaciers. *Earth Surface Processes and Landforms*. doi: [10.1002/esp.4236](https://doi.org/10.1002/esp.4236)

- Wessels RL, Kargel JS and Kieffer HH** (2002) ASTER measurement of supra-glacial lakes in the Mount Everest region of the Himalaya. *Annals of Glaciology* **34**, 399–408. doi: [10.3189/172756402781817545](https://doi.org/10.3189/172756402781817545)
- Westoby MJ** and 5 others (2014) Reconstructing historic glacial lake outburst floods through numerical modelling and geomorphological assessment: extreme events in the Himalaya. *Earth Surface Processes and Landforms* **39**(12), 1675–1692. doi: [10.1002/esp.3617](https://doi.org/10.1002/esp.3617)
- Westoby M** and 6 others (2015) Numerical modelling of glacial lake outburst floods using physically based dam-breach models. *Earth Surface Dynamics* **3**(1), 171–199. doi: [10.5194/esurf-3-171-2015](https://doi.org/10.5194/esurf-3-171-2015)
- Yamanokuchi T, Tadono T, Komori J, Kawamoto S and Tomiyama N** (2011) Temporal monitoring of supraglacial lakes on Tshojo Glacier at Bhutan. *IEEE International Geoscience and Remote Sensing Symposium, Vancouver, Canada, Paper No. 3830*.
- Zheng G** and 10 others (2021a) Increasing risk of glacial lake outburst floods from future third pole deglaciation. *Nature Climate Change*, **11**(5), 411–417. doi: [10.1038/s41558-021-01028-3](https://doi.org/10.1038/s41558-021-01028-3)
- Zheng G** and 6 others (2021b) The 2020 glacial lake outburst flood at Jinwuco, Tibet: causes, impacts, and implications for hazard and risk assessment. *The Cryosphere* **15**(7), 3159–3180. doi: [10.5194/tc-15-3159-2021](https://doi.org/10.5194/tc-15-3159-2021)